


PAUL SCHERRER INSTITUT 	Project SLS-2
Title Robust Design Strategy for SLS-2	Document identification SLS2-BJ84-001-2
Author(s) J. Bengtsson and A. Streun	Date June 6, 2017

Abstract

A robust design is insensitive to small parameter changes, i.e. engineering tolerances. For the dynamic acceptance optimization of the SLS-2 storage ring a robust design strategy is established, which is based on a complete suppression of 1st and 2nd-order sextupole terms by phase cancellation. A modification of the 7-bend achromat of SLS-2 shows better linear and nonlinear performance compared to the lattice considered as reference for the conceptual design report: the emittance (zero current) is reduced from 139 pm to 101 pm, while the robustness of dynamic aperture and momentum acceptance is significantly increased, thus strengthening confidence that off-axis injection and approx. 10 hours of beam lifetime are feasible.

This note starts with a brief description of the two lattices and the general design strategy. The beam dynamics framework is presented comprehensively although in brief. The design of the new lattice is described and its performance without and with engineering tolerances is explored, where in particular frequency maps for bare and real lattice prove the robustness. An appendix presents the same calculation for the CDR reference lattice for comparison, a collection of engineering tolerances, and a brief excursus on a round beam scheme.

Based on this work the reference lattice for the CDR will be changed soon. However with regard to technology the parameter changes are moderate and don't discard design work already done for magnets, vacuum etc.

Contents

1	Introduction	3
1.1	Requirements	3
1.2	Lattice Concept	3
1.3	Design strategy	3
1.4	The 139 pm Lattice	4
1.5	The 101 pm Lattice	5
2	Beam Dynamics Model: Analytic and Numerical Methods	6
2.1	The Hamiltonian	6
2.2	Magnetic Multipole Expansion	7
2.3	Hamiltonian Flow	8
2.4	The Poincaré Map	8
2.5	Symplectic Integrator	9
2.6	Control of the Emittance	10
2.7	Control of the Nonlinear Dynamics: Driving Terms	11
2.8	Control of the Tune Foot Print: Tune Confinement Approach	11
2.9	Longitudinal Dynamics	13
2.10	Touschek Life Time	14
3	The Baseline Lattice	15
3.1	Linear Optics	15
3.2	Nonlinear Optics: the Bare Lattice	15
3.3	Real Lattice	21
4	Conclusions and Outlook	26
	Acknowledgement	27
A	Reference Lattice Benchmarks	30
B	Engineering Tolerances	37
C	Round Beam: The Möbius Ring	38

1 Introduction

1.1 Requirements

The upgrade of the Swiss Light Source (SLS) is based on a new storage ring providing at least 30 times lower equilibrium emittance than the present 5.5 nm at 2.4 GeV, i.e. a value in the order of 150 pm (including increase due to intra-beam scattering).

An off-axis accumulation and top-up injection based on the existing booster synchrotron is included in the baseline design, whereas on-axis schemes are considered as advanced operation modes or future upgrades. Off-axis injection is realized with an orbit bump formed by three dipole kickers, where the center kicker is shielded (“anti-septum”) [1], or with a single nonlinear kicker. In both cases a minimum horizontal on-momentum aperture of $A_{x,y} \sim \pm 5$ mm is required.

Due to the high particle density in the bunch, the beam lifetime is dominated by Touschek scattering. In order to provide a beam lifetime of 5–10 hrs (already including bunch lengthening from a harmonic RF-system) a lattice momentum acceptance of $\delta^{\text{acc}} = 5\%$ is required. A summary is given by Tab. 1

Parameter	Value
On-momentum dynamic aperture $A_{x,y}$ [mm]	± 5
Off-momentum dynamic aperture δ [%]	5
Touschek lifetime [hrs]	5-10

Table 1: Beam Dynamics Requirements.

1.2 Lattice Concept

Exploiting the inverse cubical scaling of emittance with the number of lattice cells, the cell number is increased through miniaturization of magnets. This concept results in densely packed multi-bend achromat (MBA) arcs with small beam pipe dimensions [2]. In case of SLS-2 a ring lattice made built from twelve identical 7BA-arcs in 290.4 m circumference, and an inner beam pipe radius of 10 mm (magnet bore radius 13 mm) was found to provide the desired emittance reduction. However, simply scaling existing lattice designs from other places to the SLS dimensions would have resulted in an emittance in the range of 0.5–1.0 nm, which is considered insufficient. Another factor 4–5 in emittance reduction is gained from a novel type of lattice cell based on longitudinal gradient bends and anti-bends [3–10]. The 7BA of SLS-2 is made from five core cells of 5° deflection angle and two dispersion suppressor cells of 2.5° , giving a total arc deflection of 30° .

1.3 Design strategy

Optimization of non-linear optics is the main challenge for an ultra-low emittance lattice like SLS-2 in order to provide sufficient dynamic acceptance while strong non-linearities are introduced by the sextupoles needed for correction of chromaticity.

A robust solution is required. Generally, for a robust system the performance is not significantly degraded for small parameter changes. Especially, it means to not only know the solution of the nonlinear equations governing the dynamics of the system but also the derivatives.

In summary, the non-linear design strategy is to implement a higher order achromat by [11–15]:

1. introduce a unit cell with two chromatic sextupole families,

2. choose the cell tune so that all the resonance driving terms up to second order in sextupole strength are cancelled over m unit cells,
3. control the on-momentum tune footprint by three octupole families (trims) in the matching sections of the super periods; the impact is tempered by the n -fold symmetry of the lattice,
4. and control the off-momentum tune footprint by two octupole families (trims) in the unit cells.

Item 2, cancellation by phase, is explicitly shown in Tab. 2 for two relevant cases based on $m = 5$ and $m = 7$ unit cells with appropriate cell tunes. Note that the horizontal cell tune has to be rather large in order to realize small emittance, while the vertical cell tune is free basically. Also note that all regular resonances contain even multiples of the vertical tune, so the cancellation considers combinations of ν_x and $2\nu_y$.

For $m = 5$ cells a tune advance of $0.4 = 1/5$ horizontal and $0.1 = 0.5/5$ vertical provides cancellation of all 1st-order sextupole and all 2nd-order sextupole, resp. 1st-order octupole terms – except the 2nd-order term driving $2\nu_x + 2\nu_y$ resonances, which is amplified coherently.

For $m = 7$ cells a tune advance of $3/7 \approx 0.429$ horizontal and $1/7 \approx 0.143$ vertical provides cancellation of all 1st-order sextupole and all 2nd-order sextupole, resp. 1st-order octupole terms.

Eventually, for a realistic design, space and engineering considerations, etc. impose additional, often conflicting constraints requiring compromises for the performance and technical design. In conclusion, to design a magnetic lattice for a state-of-the-arts ring-based synchrotron light source, is a nontrivial, nonlinear optimization problem.

Higher Order Achromats

Cell	ν_x	ν_y		First Order						Second Order				Third Order				
				Geometric				Chromatic		Geometric				Geometric				
				ν_x	$3\nu_x$	$\nu_x-2\nu_y$	$\nu_x+2\nu_y$	$2\nu_x$	$2\nu_y$	$4\nu_x$	$4\nu_y$	$2\nu_x-2\nu_y$	$2\nu_x+2\nu_y$	$5\nu_x$	$\nu_x-4\nu_y$	$\nu_x+4\nu_y$	$3\nu_x-2\nu_y$	$3\nu_x+2\nu_y$
1	0.400	0.100	2/5, 0.5/5	0.40	1.20	0.20	0.60	0.80	0.20	1.60	0.40	0.60	1.00	2.00	0.00	0.80	1.00	1.40
2	0.800	0.200		0.80	2.40	0.40	1.20	1.60	0.40	3.20	0.80	1.20	2.00	4.00	0.00	1.60	2.00	2.80
3	1.200	0.300		1.20	3.60	0.60	1.80	2.40	0.60	4.80	1.20	1.80	3.00	6.00	0.00	2.40	3.00	4.20
4	1.600	0.400		1.60	4.80	0.80	2.40	3.20	0.80	6.40	1.60	2.40	4.00	8.00	0.00	3.20	4.00	5.60
5	2.000	0.500		2.00	6.00	1.00	3.00	4.00	1.00	8.00	2.00	3.00	5.00	10.00	0.00	4.00	5.00	7.00

Cell	ν_x	ν_y		Geometric				Chromatic		Geometric				Geometric				
				ν_x	$3\nu_x$	$\nu_x-2\nu_y$	$\nu_x+2\nu_y$	$2\nu_x$	$2\nu_y$	$4\nu_x$	$4\nu_y$	$2\nu_x-2\nu_y$	$2\nu_x+2\nu_y$	$5\nu_x$	$\nu_x-4\nu_y$	$\nu_x+4\nu_y$	$3\nu_x-2\nu_y$	$3\nu_x+2\nu_y$
				1	0.429	0.143	3/7, 1/7	0.43	1.29	0.14	0.71	0.86	0.29	1.71	0.57	0.57	1.14	2.14
2	0.857	0.286		0.86	2.57	0.29	1.43	1.71	0.57	3.43	1.14	1.14	2.29	4.29	-0.29	2.00	2.00	3.14
3	1.286	0.429		1.29	3.86	0.43	2.14	2.57	0.86	5.14	1.71	1.71	3.43	6.43	-0.43	3.00	3.00	4.71
4	1.714	0.571		1.71	5.14	0.57	2.86	3.43	1.14	6.86	2.29	2.29	4.57	8.57	-0.57	4.00	4.00	6.29
5	2.143	0.714		2.14	6.43	0.71	3.57	4.29	1.43	8.57	2.86	2.86	5.71	10.71	-0.71	5.00	5.00	7.86
6	2.571	0.857		2.57	7.71	0.86	4.29	5.14	1.71	10.29	3.43	3.43	6.86	12.86	-0.86	6.00	6.00	9.43
7	3.000	1.000		3.00	9.00	1.00	5.00	6.00	2.00	12.00	4.00	4.00	8.00	15.00	-1.00	7.00	7.00	11.00

Table 2: Resonance Cancellations for $\bar{\nu}_{\text{cell}} = [3/7, 1/7]$ vs. $[2/5, 0.5/5]$.

1.4 The 139 pm Lattice

The reference lattice for the conceptual design report is a period $n = 12$ lattice based on 7BA-arcs and 5.4 m straight sections providing a zero current emittance of 139 pm.

Considering a phase cancellation based on the $m = 5$ core cells of the achromat, a cell tune advance of $0.4 = 1/5$ horizontal and $0.1 = 0.5/5$ vertical provides cancellation of 1st and 2nd-order terms except

the one related to $2\nu_x + 2\nu_y$ resonances, as shown in Tab. 2.

A Multi-Objective Genetic Algorithm (MOGA) had been established to optimize the nonlinear optics: dynamic apertures for $\delta = 0, \pm 3\%$ and the size of the tune footprint, i.e. amplitude dependent tune shifts (ADTS) and chromatic tune shifts, were chosen as objectives for the minimizer [16, 17].

The vertical cell tune was included for the MOGA numerical optimizations which lead to a change of ν_y from 0.1 to $0.083 \approx 0.5/6$, indicating that the cancellation pattern implicitly switched to a 6-cell base for the vertical.

Dynamic acceptances as large as required were achieved for the bare (i.e. error free) lattice, but further analysis revealed that the solution is not robust, which is mainly due to the incomplete 2nd-order cancellation: application of the same benchmarks used for the robust approach and solution presented below are shown in Appendix A.

1.5 The 101 pm Lattice

A complete 2nd-order cancellation based on $m = 7$ cells is achieved at a cell tune advance of $3/7 \approx 0.429$ horizontal and $1/7 \approx 0.143$, see Tab. 2. However using 7 cells in a 7BA requires to include the dispersion suppressor and matching cells into the cancellation pattern. This is only feasible to a certain extent, since optical functions deviate in these regions. In particular there is no dispersion, so complete cancellation cannot be achieved for the chromatic resonance modes. However, the cancellation does not need to be perfect. Anyway, some detuning of the regular pattern has to be accepted in order to control ADTS and matching cell quadrupole contributions to second order chromaticity.

On the other hand, the reduction of horizontal cell tune provides a significant further reduction of emittance down to 101 pm. Thus the performance of the lattice is increased both with respect to brightness and to dynamic acceptance (i.e. injection efficiency and beam lifetime). Note, however, that the lattice studied here contains a few more octupoles than space is available and thus has to be considered an academic exercise so far, but there is confidence to remove these conflicts soon.

Fig. 1 shows the optical functions of the lattice 101pm_s7o7_a, which look quite similar to the 139 pm lattice. The matching section has been redesigned replacing the quadrupole triplets by quadruplets, which allows a variation of global tunes without affecting the achromat and even led to a slight increase of straight length to 5.52 m. Table 3 displays the most important parameters of both lattices in comparison to the present SLS. Note, due to the anti-bends, the total *absolute* deflection angle of the upgrade ring amounts to more than 360° , and the momentum compaction factor (MCF) becomes negative. Parameters are for a lattice with 12 identical arcs disregarding possible superbends. The SLS-lattice however includes 3 superbends and the FEMTO insertion for laser beam slicing, which also increases the absolute deflection angle to $> 360^\circ$.

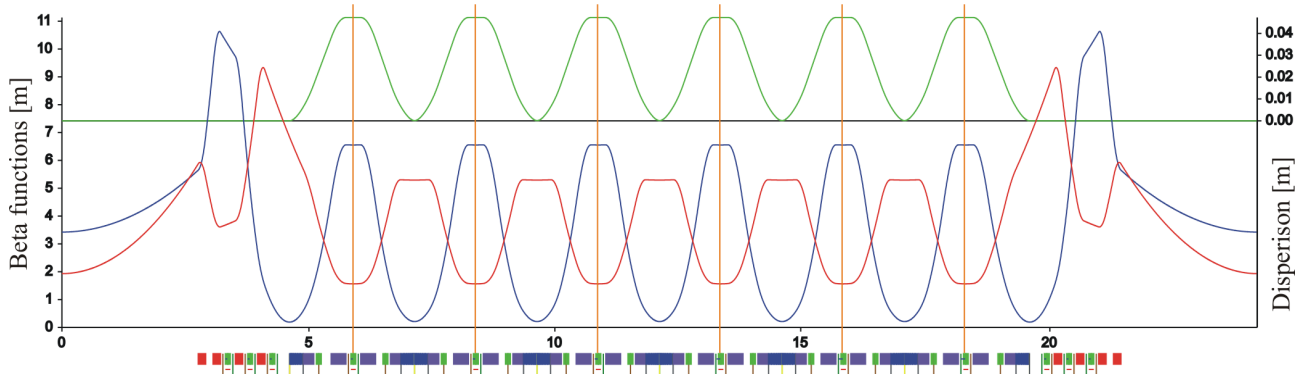


Figure 1: Optical functions of the 101 pm lattice. The orange lines mark the five core cells of the 7BA.

Table 3: Parameters of the present SLS lattice and the 139 pm and 101 pm SLS-2 lattices

		SLS	139 pm	101 pm
Circumference	C [m]	288.0	290.4	290.4
Total absolute deflection	$\Sigma \phi $ [°]	375.0	584.6	561.6
Working point	$\nu_{x,y}$	20.4, 8.7	37.2, 10.3	39.2, 15.3
Chromaticity	$\xi_{x,y}$	-67, -21	-67, -40	-95, -35
Momentum compaction	α	$6.04 \cdot 10^{-4}$	$-1.36 \cdot 10^{-4}$	$-1.31 \cdot 10^{-4}$
Horizontal emittance	ε [pm]	5670	139	101
Energy spread	$\sigma_{\Delta E/E}$	$0.88 \cdot 10^{-3}$	$1.03 \cdot 10^{-3}$	$1.01 \cdot 10^{-3}$
Energy loss/turn	ΔE_{rad} [keV]	549	570	545
Damping times	$\tau_{x,y,s}$ [ms]	8.5, 8.4, 4.2	4.6, 8.2, 6.6	5.0, 8.5, 6.7

2 Beam Dynamics Model: Analytic and Numerical Methods

2.1 The Hamiltonian

The relativistic Hamiltonian for a charged particle in an external electromagnetic field for the co-moving system customarily used to model particle accelerators is ($\bar{x} = [x, p_x, y, p_y, c_0 t, p_t]$) [15]

$$H(\bar{x}; s) = -(1 + h_0 x) \left[\frac{q}{p_0} A_s + \sqrt{1 + \frac{2}{\beta_0} p_t + p_t^2 - \left(p_x - \frac{q}{p_0} A_x \right)^2 - \left(p_y - \frac{q}{p_0} A_y \right)^2} \right] + q\Phi \quad (1)$$

where $h_0(s)$ is the local curvature, p_t the canonical longitudinal momentum coordinate and β, γ the relativistic factors

$$h_0(s) \equiv \frac{1}{\rho_0(s)}, \quad p_t \equiv \frac{E - E_0}{p_0 c_0}, \quad \gamma = \frac{1}{\sqrt{1 - \beta^2}} = \frac{E}{m_0 c_0^2}. \quad (2)$$

Hence, in the limit of negligible classical radiation (no radiation damping) and no quantum fluctuations (no photon emission), e.g. proton and ion accelerators, the phase-space dynamics is like for an incompressible fluid.

For ultra relativistic beams $\beta_0 \rightarrow 1$, the momentum deviation is sometimes used instead

$$\delta \equiv \frac{p - p_0}{p_0}, \quad (1 + \delta)^2 = \frac{E^2 - (m_0 c_0^2)^2}{(p_0 c_0)^2} = \frac{(E - E_0)^2 + 2E_0(E - E_0) + (p_0 c_0)^2}{(p_0 c_0)^2} = 1 + \frac{2}{\beta_0} p_t + p_t^2 \approx (1 + p_t)^2 \quad (3)$$

which leads to

$$\begin{aligned} H(\bar{x}; s) &= -(1 + h_0 x) \left[\frac{q}{p_0} A_s + \sqrt{(1 + \delta)^2 - \left(p_x - \frac{q}{p_0} A_x \right)^2 - \left(p_y - \frac{q}{p_0} A_y \right)^2} \right] + q\Phi \\ &= \frac{p_x^2 + p_y^2}{2(1 + \delta)} - h_0 x - (1 + h_0 x) \frac{q}{p_0} A_s + \dots \end{aligned} \quad (4)$$

The expanded expression is the small angle approximation; which is “exact” (not expanded) in δ .

Alternatively, one may introduce

$$p_E \equiv \frac{E - E_0}{E_0} \quad (5)$$

for which

$$(1 + \delta)^2 = \frac{E^2 - (m_0 c_0^2)^2}{(p_0 c_0)^2} = \frac{E_0^2}{(p_0 c_0)^2} \frac{(E - E_0)^2 + 2E_0(E - E_0) + (p_0 c_0)^2}{E_0^2} = 1 + \frac{2}{\beta_0^2} p_E + \frac{1}{\beta_0^2} p_E^2. \quad (6)$$

However, the initial Hamiltonian would then be scaled with energy E_0 vs. p_0 and as a result the transverse momenta as well.

2.2 Magnetic Multipole Expansion

The magnetic multipole expansion is introduced by [15]

$$\begin{aligned} B_y(s) + iB_x(s) &= (B\rho) \sum_{n=1}^{\infty} (ia_n(s) + b_n(s)) (re^{i\varphi})^{n-1} \\ &= (B\rho) \sum_{n=1}^{\infty} (ia_n(s) + b_n(s)) (x + iy)^{n-1}. \end{aligned} \quad (7)$$

with the *magnetic rigidity*

$$(B\rho) \equiv \frac{p}{q}. \quad (8)$$

The vector potential is obtained from the Poincaré gauge, $\bar{r} \cdot \bar{A} = 0$ [18]:

$$\bar{A}(\bar{r}, t) = -\bar{r} \times \int_0^1 \bar{B}(u\bar{r}, t) u du, \quad \phi = -\bar{r} \cdot \int_0^1 \bar{B}(u\bar{r}, t) u du \quad (9)$$

The curl $\bar{B} \equiv \nabla \times \bar{A}$ in the curvilinear co-moving system is [19]

$$B_x = \frac{\partial_z A_y - \partial_y A_z}{1 + h_0(s)x}, \quad B_y = \frac{h(s)A_s}{1 + h_0(s)x} + \partial_x A_s - \frac{\partial_s A_x}{1 + h_0(s)x}, \quad B_z = \partial_y A_x - \partial_x A_y. \quad (10)$$

2.3 Hamiltonian Flow

Hamilton's equations are an infinitesimal map

$$x' = [-H, x] = \partial_{p_x} H, \quad p'_x = [-H, p_x] = -\partial_x H. \quad (11)$$

with the Poisson bracket defined by

$$[f, g] \equiv \sum_{k=1}^6 (\partial_{q^k} f \partial_{p_k} g - \partial_{p_k} f \partial_{q^k} g). \quad (12)$$

The flow is symplectic¹, i.e., the symplectic 2-form

$$\omega(q^i, p_i) \equiv -dq^r \wedge dp_r = \frac{1}{2} \omega_{rs} dq^r dp_s, \quad d\omega = 0, \quad \omega_{ij} \equiv \begin{bmatrix} 0 & -I_n \\ I_n & 0 \end{bmatrix} \quad (13)$$

is an (differential) invariant

$$\mathcal{L}_{-H}\omega = 0 \quad (14)$$

and it follows that the phase-space volume is preserved (Liouville's theorem)

$$\omega^n(q^i, p_i) = \left(\sum_k dq^k \wedge dp_k \right)^n = \prod_k dq^k \wedge dp_k + \dots = \text{const.} \quad (15)$$

The inverse matrix is obtained from

$$\Omega^{ir} \omega_{rj} = \delta_j^i, \quad \Omega^{ij} = \begin{bmatrix} 0 & I_n \\ -I_n & 0 \end{bmatrix} \quad (16)$$

and the corresponding (global) symplectic (quadratic) form

$$\Omega(\bar{x}_1, \bar{x}_2) \equiv \bar{x}_1^T \Omega \bar{x}_2 \quad (17)$$

is invariant under linear symplectic transformations

$$\bar{x}_1^T \Omega \bar{x}_2 \rightarrow (M\bar{x}_1)^T \Omega M\bar{x}_2 = \bar{x}_1^T M^T \Omega M \bar{x}_2 \quad (18)$$

for which

$$M^T \Omega M = \Omega, \quad (19)$$

also known as symplectic matrices.

Note that the Poisson bracket can be defined as

$$[f, g] \equiv \Omega^{rs} \partial_r f \partial_s g. \quad (20)$$

2.4 The Poincaré Map

The (finite) Poincaré map can be expressed as a Lie series ($\bar{x} \equiv [q^i, p_i]$) [20]

$$\bar{x}_1 = \mathcal{M}\bar{x}_0 = e^{\mathcal{L}_{-H}} \bar{x}_0 \equiv \sum_{k=0}^{\infty} \frac{\mathcal{L}_{-H}^k}{k!} \bar{x}_0 = \left(1 - \frac{\mathcal{L}_{-H}}{1!} + \frac{\mathcal{L}_{-H}^2}{2!} + \dots \right) \bar{x}_0 \quad (21)$$

¹Greek for intertwined

where the Lie derivative is the Poisson bracket:

$$\mathcal{L}_f g(\bar{x}) = [f, g]. \quad (22)$$

Linearizing by expanding the Hamiltonian to second order in the phase space coordinates gives [15]

$$H_2(\bar{x}; s) = \frac{p_x^2 + p_y^2}{2(1+\delta)} - b_1(s)x\delta + \frac{b_1^2(s)}{2}x^2 + \frac{b_2(s)}{2}(x^2 - y^2) + O(\bar{x})^3. \quad (23)$$

For a periodic system, the homogeneous term is removed by introducing a momentum dependent fixed point

$$M\bar{\eta}^{(1)}\delta = \bar{\eta}^{(1)}\delta \quad (24)$$

where $\bar{\eta}^{(1)}$ is the linear dispersion function.

The motion around the fixed point can then be integrated for a piecewise constant potential, leading to the corresponding transport matrices, which are symplectic, see Eq. 19. The linear one-turn map is obtained by concatenation, i.e., matrix multiplication, and can be diagonalized

$$M = ARA^{-1}, \quad R = \begin{bmatrix} \cos(2\pi\nu_x) & \sin(2\pi\nu_x) \\ -\sin(2\pi\nu_x) & \cos(2\pi\nu_x) \end{bmatrix}, \quad A = \begin{bmatrix} \sqrt{\beta_x} & 0 \\ -\frac{\alpha_x}{\sqrt{\beta_x}} & \frac{1}{\sqrt{\beta_x}} \end{bmatrix} \quad (25)$$

where $[\alpha_x, \beta_x, 2\pi\nu_x]$ are the Courant & Snyder parameters [21]. The system is stable for

$$|\text{Tr}\{M\}| < 2. \quad (26)$$

Similarly, the linear optics functions along the lattice are obtained from

$$M_{01} = A_1 R_{01} A_0^{-1} \quad \text{with} \quad (27)$$

$$R_{01} = \begin{bmatrix} \cos(\mu_x) & \sin(\mu_x) \\ -\sin(\mu_x) & \cos(\mu_x) \end{bmatrix}, \quad A_k = \begin{bmatrix} \sqrt{\beta_{x,k}} & 0 \\ -\frac{\alpha_{x,k}}{\sqrt{\beta_{x,k}}} & \frac{1}{\sqrt{\beta_{x,k}}} \end{bmatrix}, \quad A_k^{-1} = \begin{bmatrix} \frac{1}{\sqrt{\beta_{x,k}}} & 0 \\ \frac{\alpha_{x,k}}{\sqrt{\beta_{x,k}}} & \sqrt{\beta_{x,k}} \end{bmatrix}. \quad (28)$$

The linear action-angle variables are

$$2J_x \equiv \|\tilde{x}\|^2 = \tilde{x}^T \tilde{x} = \tilde{q}_x^2 + \tilde{p}_x^2, \quad \phi \equiv \arctan\left(\frac{\tilde{p}_x}{\tilde{q}_x}\right) \quad (29)$$

with the Floquet space vector

$$\tilde{x} = A^{-1}\bar{x}, \quad \tilde{x} \equiv [\tilde{q}_x, \tilde{p}_x]. \quad (30)$$

Similar expressions hold for the vertical and longitudinal planes.

2.5 Symplectic Integrator

The expanded Hamiltonian from Eq. 4 can be split into a “drift” and “kick” part

$$H(\bar{x}; s) = H_d(p_x, p_y; s) + H_k(x, y; s) \quad (31)$$

where

$$H_d(p_x, p_y; s) \equiv \frac{p_x^2 + p_y^2}{2(1+\delta)}, \quad H_k(x, y; s) \equiv -h_0(s)x - (1+h_0(s)x)\frac{q}{p_0}A_s(x, y; s) \quad (32)$$

for which Hamilton's equations can be integrated to obtain the corresponding maps

$$\mathcal{M}_d(s) \equiv e^{s\mathcal{L}-H_d}, \quad \mathcal{M}_k(s) \equiv e^{s\mathcal{L}-H_k}. \quad (33)$$

A 2nd order symplectic integrator is obtained by

$$\mathcal{M}_2 = \mathcal{M}_d\left(\frac{L}{2}\right) \mathcal{M}_k(L) \mathcal{M}_d\left(\frac{L}{2}\right) + O(L)^3 = \left(\mathcal{M}_d\left(\frac{L}{2n}\right) \mathcal{M}_k\left(\frac{L}{n}\right) \mathcal{M}_d\left(\frac{L}{2n}\right)\right)^n + O\left(\frac{L}{n}\right)^3 \quad (34)$$

where the second expression is for n integration steps. Given an order $2n$ symplectic integrator, an order $2n + 2$ is obtained by [22–24]

$$\mathcal{M}_{2n+2} = \mathcal{M}_{2n}(\alpha_2 L) \mathcal{M}_{2n}(\alpha_1 L) \mathcal{M}_{2n}(\alpha_2 L) + O(L)^{2n+3} \quad (35)$$

where

$$\alpha_1 \equiv -\frac{2^{\frac{1}{2n+1}}}{2 - 2^{\frac{1}{2n+1}}}, \quad \alpha_2 \equiv \frac{1}{2 - 2^{\frac{1}{2n+1}}}. \quad (36)$$

For numerical simulations (tracking) the equations of motion are integrated with a 4th-order symplectic integrator; i.e. a $O(\Delta s^5)$ error is left for each integration step, whereas the phase-space volume is conserved. The latter is crucial for modeling on the time scale of a damping time (approx. 10^3 turns).

2.6 Control of the Emittance

The horizontal emittance is controlled by controlling the linear dispersion action

$$\mathcal{H}_x \equiv \|\tilde{\eta}\|^2 = \tilde{\eta}^T \tilde{\eta}, \quad \tilde{\eta} = A^{-1} \bar{\eta}, \quad \bar{\eta} \equiv [\eta_x, \eta'_x]. \quad (37)$$

In particular, the emittance is a dynamic equilibrium between damping τ and diffusion D_δ due to classical radiation and quantum fluctuations from photon emission [25]

$$\varepsilon_{x,y} = \tau_{x,y} \langle \mathcal{H}_{x,y} D_\delta \rangle, \quad \sigma_\delta^2 = \tau_\delta \langle D_\delta \rangle = \frac{C_q \left\langle \frac{1}{\rho^3} \right\rangle \gamma_0^2}{J_\delta \left\langle \frac{1}{\rho^2} \right\rangle} \simeq \frac{C_u h \nu_c}{2 J_\delta E_0}, \quad C_q \equiv \frac{3 C_u \hbar}{4 m_e c_0}, \quad C_u \equiv \frac{55}{24 \sqrt{3}} \quad (38)$$

with

$$D_\delta \simeq \frac{C_u \langle P_\gamma \rangle h \nu_c}{4 N_b q_e E_0^2} = \frac{C_u U_0 h \nu_c}{4 T_0 E_0^2}, \quad \langle P_\gamma \rangle = U_0 I_b = \frac{N_b q_e U_0}{T_0} \quad (39)$$

and

$$\tau_\delta = \frac{2 N_b q_e E_0}{J_\delta \langle P_\gamma \rangle} = \frac{2 T_0 E_0}{J_\delta U_{\text{tot}}}, \quad J_x \tau_x = J_y \tau_y = J_\delta \tau_\delta, \quad J_x + J_y + J_\delta = 4 \quad (40)$$

where τ is the damping time, \mathcal{H} the linear dispersion action, D the diffusion coefficient, J the partition number, T_0 [s] the revolution time, E_0 [eV] the beam energy, U_0 [eV] the radiated energy by an electron per turn, $\langle P_\gamma \rangle$ [W] the total radiated power, I_b [A] the beam current, N_b [As] the beam charge, $h \nu_c$ [eV] the critical photon energy, and q_e [As] the electron charge. For dipoles without gradient

$$J_x \approx J_y \approx 1, \quad J_\delta \approx 2. \quad (41)$$

The factor 2 between the transverse vs. longitudinal plane is because the action, rather than the amplitude, is being damped for the former.

2.7 Control of the Nonlinear Dynamics: Driving Terms

For the nonlinear case, a Taylor map is extracted from the symplectic integrator by automatic differentiation via a C++ implementation of ditto. Under quite general conditions, by using Lie series, it can be factorized [26, 27]

$$\mathcal{M} = e^{\mathcal{L}-h_2} e^{\mathcal{L}-h_3} e^{\mathcal{L}-h_4} \dots = M e^{\mathcal{L}-h_3} e^{\mathcal{L}-h_4} \dots \quad (42)$$

where M is a linear map and $h_n(\bar{x})$ are homogenous polynomials in the phase-space coordinates of degree n . For a lattice with a discrete set of e.g. thin sextupoles $(b_3L)_k$ to leading order

$$h_3 \equiv \sum_{\bar{I}} h_{\bar{I}} (2J_x)^{\frac{i_1+i_2}{2}} (2J_y)^{\frac{i_3+i_4}{2}} \delta^{i_5} e^{i[(i_1+i_2)\phi_x+(i_3+i_4)\phi_y]}, \quad \bar{I} \equiv [i_1, i_2, i_3, i_4, i_5] \quad (43)$$

where

$$h_{\bar{I}} \sim \sum_{k=1}^N (b_3L)_k (\beta_{x,k})^{\frac{i_1+i_2}{2}} (\beta_{y,k})^{\frac{i_3+i_4}{2}} \eta_{x,k}^{i_5} e^{i[(i_1+i_2)\mu_{x,k}+(i_3+i_4)\mu_{y,k}]} \quad (44)$$

The Lie series approach provides a recursive formulation which can be automated to arbitrary order [28]. For the SSC conceptual design analytic expressions were worked out up to decapoles (for realistic representation of super-conducting magnets) [29], and for the SLS conceptual design to second order in the sextupole strengths [15].

The map can be written in normal form by a Lie transform $g(\bar{\phi}, \bar{J}; \delta)$ (a canonical transformation obtained by perturbation theory) so that $K(\bar{J}; \delta)$ only depends on the linear action [28, 30]

$$\mathcal{M} = e^{\mathcal{L}-H(\bar{\phi}, \bar{J}; \delta)} = \mathcal{A} e^{\mathcal{L}-g(\bar{\phi}, \bar{J}; \delta)} e^{\mathcal{L}-K(\bar{J}; \delta)} e^{\mathcal{L}-g(\bar{\phi}, \bar{J}; \delta)} \mathcal{A}^{-1} \quad (45)$$

where \mathcal{A} is a linear map and $[\bar{\phi}, \bar{J}]$ the action-angle variables for the linear system. The tune, including amplitude dependant tune shift and chromaticity, is then obtained from

$$\bar{\nu}(\bar{J}; \delta) = \frac{1}{2\pi} \partial_{\bar{J}} K(\bar{J}; \delta) \quad (46)$$

whereas $g(\bar{\phi}, \bar{J}; \delta)$ describes the distortions of the linear optics functions.

2.8 Control of the Tune Foot Print: Tune Confinement Approach

The tune foot print is obtained from Eq. 46

$$\bar{\nu} = \frac{1}{2\pi} \partial_{\bar{J}} K \quad (47)$$

where

$$\begin{aligned} K(\bar{J}; \delta) = & k_{11000} J_x + k_{00110} J_y + k_{22000} J_x^2 + k_{00220} J_y^2 + k_{11110} J_x J_y \\ & + k_{33000} J_x^3 + k_{00330} J_y^3 + k_{h22110} J_x^2 J_y + k_{11220} J_x J_y^2 \\ & + k_{44000} J_x^4 + k_{00440} J_y^4 + k_{22220} J_x^2 J_y^2 + k_{33110} J_x^3 J_y + k_{11330} J_x J_y^3 \\ & + k_{11001} J_x \delta + k_{00111} J_y \delta \\ & + k_{11002} J_x \delta^2 + k_{00112} J_y \delta^2 + k_{22001} J_x^2 \delta + k_{00221} J_y^2 \delta + k_{11111} J_x J_y \delta \\ & + k_{22002} J_x^2 \delta^2 + k_{00222} J_y^2 \delta^2 + k_{11112} J_x J_y \delta^2 + \dots \end{aligned} \quad (48)$$

which gives

$$\begin{aligned}
\nu_x &= -\frac{1}{2\pi}\partial_{J_x}K = -\frac{1}{2\pi} \left(k_{11000} + 2k_{22000}J_x + k_{11110}J_y + 3k_{33000}J_x^2 + 2k_{22110}J_xJ_y + k_{11220}J_y^2 \right. \\
&\quad + 4k_{44000}J_x^3 + 2k_{22220}J_xJ_y^2 + 3k_{33110}J_xJ_y + k_{11330}J_y^3 \\
&\quad \left. + k_{11001}\delta + k_{11002}\delta^2 + 2k_{22001}J_x\delta + k_{11111}J_y\delta + 2k_{22002}J_x\delta^2 + k_{11112}J_y\delta^2 + \dots \right), \\
\nu_y &= -\frac{1}{2\pi}\partial_{J_y}K = -\frac{1}{2\pi} \left(k_{00110} + 2k_{00220}J_y + k_{11110}J_x + 3k_{00330}J_y^2 + k_{22110}J_x^2 + 2k_{11220}J_xJ_y \right. \\
&\quad + 4k_{00440}J_y^3 + 2k_{22220}J_x^2J_y + k_{33110}J_x^3 + 3k_{11330}J_xJ_y^2 \\
&\quad \left. + k_{00111}\delta + k_{00112}\delta^2 + 2k_{00221}J_y\delta + k_{11111}J_x\delta + 2k_{00222}J_y\delta^2 + k_{11112}J_x\delta^2 + \dots \right). \tag{49}
\end{aligned}$$

The surface area is

$$\begin{aligned}
\iiint |\Delta\nu_x| |\Delta\nu_y| dJ_x dJ_y d\delta &= \iiint \sqrt{\Delta\nu_x^2 \Delta\nu_y^2} dJ_x dJ_y d\delta \\
&= \iiint \frac{1}{4\pi^2} \sqrt{(\partial_{J_x}K - h_{11000})^2 (\partial_{J_y}K - h_{00110})^2} dJ_x dJ_y d\delta \\
&\leq \iiint \frac{1}{4\pi^2} (4h_{22000}^2 J_x^2 + h_{11110}^2 J_y^2 + h_{11001}^2 \delta^2 + \dots)^{1/2} \\
&\quad \times (4h_{00220}^2 J_y^2 + h_{11110}^2 J_x^2 + h_{00111}^2 \delta^2 + \dots)^{1/2} dJ_x dJ_y d\delta. \tag{50}
\end{aligned}$$

where the Cauchy-Schwarz inequality has been used for the last step.

The last expression, also known as a L^2 -norm to mathematicians, has been the guiding principle for a robust design of SLS [15,31]. Analytic expressions for the resonance driving and tune foot print terms to second order in the sextupole strength, only requiring knowledge of the linear optics functions, were ported to OPA [32] in order to streamline the iterative design process for control of:

$$\text{linear optics} \Leftrightarrow \text{nonlinear dynamics.}$$

The multipole strength is controlled by including higher order terms. Clearly, at some magnitude for the multipole strengths, the higher order terms no longer taper off, which gives an upper bound for the nonlinear corrections. Having determined this upper bound by a higher order evaluation of the resonance driving terms and the tune foot print, one can then simplify the nonlinear optimizations, i.e. solving, in a least-square sense an over-constrained nonlinear system of polynomial equations for the multipole strength.

So, as a refinement, instead of minimizing the L^2 norm for the power series coefficients, one may minimize the tune footprint directly; i.e., by balancing the nonlinear terms. In other words, attempt to improve the stability by adding nonlinearity. In particular, because the L^2 norm leads to a quite stiff nonlinear system of algebraic equations (e.g. NSLS-II [33]), unless octupoles are introduced, as it was done for MAX-IV [11]. The MAX-IV design is not only robust but also conservative [11], i.e. it can be pushed during the facility's life cycle [14].

As an example Tab. 4 shows the Lie generators (driving terms) for the 101 pm lattice of SLS-2 (see below). In conclusion, the here presented solution was obtained by suppressing the resonance driving and tune foot print terms to $\sim 1 \times 10^{-8}$, evaluated at some representative transverse amplitude and momentum aperture, and with a heuristic scale factor between the latter and former terms, since they have different units.

One concern with regard to tune confinement is a ‘‘folding’’ of the tune foot print, see ref. [34]. In particular, the KAM stability theorem for Hamiltonian systems [35–37] requires that it is non-degenerate

$$\det \{ \partial_{\bar{J}} \bar{\nu} \} = \det \{ \partial_{\bar{J} \bar{J}} H(\bar{J}) \} \neq 0. \tag{51}$$

Hence, it is desirable to keep such points outside the physical aperture. On the other hand, from a phenomenological point of view, it is clear that resonance driving terms are required for such points to be problematic. Furthermore, for electrons there is radiation damping, i.e. it is not a pure Hamiltonian system.

2.9 Longitudinal Dynamics

For 2.5 degrees-of-freedom (δ treated as a parameter not as a dynamic variable), introducing phase-space coordinates relative to the momentum dependent fixed point from Eq. 24,

$$\bar{x} \rightarrow \bar{x} + \bar{\eta}^{(1)}\delta + \dots \quad (52)$$

into the Hamiltonian from Eq. 23 gives

$$\begin{aligned} H(\bar{x}; s) &= \frac{p_x^2 + \eta_x^{(1)'}\delta^2}{2(1+\delta)} - b_1 \left(x + \eta_x^{(1)}\delta \right) \delta + \frac{b_1^2 + b_2}{2} \left(x^2 + 2x\eta_x^{(1)}\delta + \eta_x^{(1)2}\delta^2 \right) \\ &+ \frac{b_3}{3} \left(x^3 + 3x^2\eta_x^{(1)}\delta + 3x\eta_x^{(1)2}\delta^2 + \eta_x^{(1)3}\delta^3 \right) \\ &+ \frac{b_4}{4} \left(x^4 + 4x^3\eta_x^{(1)}\delta + 6x^2\eta_x^{(1)2}\delta^2 + 4x^3\eta_x^{(1)3}\delta^3 + \eta_x^{(1)4}\delta^4 \right) + \dots \end{aligned}$$

The time of flight is obtained from

$$\begin{aligned} c_0 t' = \partial_\delta H &= \eta_x^{(1)'}\delta - b_1 \left(x + 2\eta_x^{(1)}\delta \right) + (b_1^2 + b_2) \left(x + \eta_x^{(1)}\delta \right) \eta_x^{(1)} \\ &+ b_3 \left(x^2\eta_x^{(1)} + 2x\eta_x^{(1)2}\delta + \eta_x^{(1)3}\delta^2 \right) \\ &+ b_4 \left(x^3\eta_x^{(1)} + 3x^2\eta_x^{(1)2}\delta + 3x^3\eta_x^{(1)3}\delta^2 + \eta_x^{(1)4}\delta^3 \right) + \dots \end{aligned}$$

The time of flight depends on the transverse betatron amplitude as well.

By introducing action-angle variables from Eq. 29, the Hamiltonian for the transverse dynamics simplifies to [19]

$$K(\bar{\phi}, \bar{J}) = 2\pi(\nu_x J_x + \nu_y J_y) + \left(\xi_x^{(1)} J_x + \xi_y^{(1)} J_y \right) \delta + \dots \quad (53)$$

with Hamilton's equations

$$\begin{aligned} J'_x &= \partial_{-\phi_x} K = 0, & \phi'_x &= \partial_{J_x} K = 2\pi\nu_x + \xi_x^{(1)}\delta, \\ J'_y &= \partial_{-\phi_y} K = 0, & \phi'_y &= \partial_{J_y} K = 2\pi\nu_y + \xi_y^{(1)}\delta, \\ c_0 t' &= \partial_\delta K = \xi_x^{(1)} J_x + \xi_y^{(1)} J_y. \end{aligned}$$

i.e., the path dependence with transverse amplitude originates from the (linear) chromaticity, because the flow is symplectic.

The Hamiltonian for the longitudinal dynamics is [51]

$$H(\phi_\delta, \delta) = \frac{h\eta^{(1)}\delta^2}{2} + \frac{h\eta^{(2)}\delta^3}{3} + \frac{eV_{\text{rf}}}{2\pi E_0} [\cos(\phi_\delta + \phi_0) + \phi_\delta \sin(\phi_0)] \quad (54)$$

where E_0 is the beam energy, V_{rf} the RF cavity voltage, h the harmonic number, ϕ_0 the synchronous phase, e the electron charge, and η the phase slip factor

$$\eta \equiv \frac{E_0}{T_0} \frac{dT_0}{dE} = \eta^{(1)} + \eta^{(2)} \frac{dE}{E} + \dots \quad (55)$$

where T_0 is the revolution time. To leading order the phase slip factor is

$$\eta^{(1)} = \frac{1}{L} \int_0^L \frac{\eta_x^{(1)}(s)}{\rho(s)} ds - \frac{1}{\beta_0^2 \gamma_0^2} \quad (56)$$

where L is the length of the structure, and β_0, γ_0 are the relativistic factors.

Similarly, the momentum compaction is defined by

$$\alpha \equiv \frac{p_0}{L} \frac{dL}{dp} = \alpha^{(1)} + \alpha^{(2)} \delta + \dots \quad (57)$$

and to leading order

$$\alpha^{(1)} = \frac{1}{L} \int_0^L \frac{\eta_x^{(1)}(s)}{\rho(s)} ds, \quad \alpha^{(2)} = \frac{1}{L} \int_0^L \left(\frac{2\eta_x^{(2)}(s)}{\rho(s)} + \eta_x^{(1) \prime 2}(s) \right) ds. \quad (58)$$

They are related by

$$\eta^{(1)} = \alpha^{(1)} - \frac{1}{\beta_0^2 \gamma_0^2}. \quad (59)$$

Collecting the results, to leading order the Hamiltonian is

$$H(\bar{J}, \bar{\phi}, \phi_\delta, \delta) = \frac{h\eta^{(1)}\delta^2}{2} + \frac{h\eta^{(2)}\delta^3}{3} + \frac{eV_{\text{rf}}}{2\pi E_0} [\cos(\phi_\delta + \phi_0) + \phi_\delta \sin(\phi_0)] + \left(\xi_x^{(1)} J_x + \xi_y^{(1)} J_y \right) \delta + \dots \quad (60)$$

2.10 Touschek Life Time

The beam half life time due to Touschek scattering is given by [38–40]

$$\frac{1}{T} = \frac{r_e^2 c_o N_e}{8\pi \gamma^3 \sigma_s C} \oint \frac{F \left[\left(\frac{\delta_{\text{acc}}(s)}{\gamma \sigma_{x'}(s)} \right)^2 \right]}{\sigma_x(s) \sigma_y(s) \sigma_{x'}(s) \delta_{\text{acc}}^2(s)} ds \quad (61)$$

$$\text{where } \sigma_{x'}(s) = \frac{\varepsilon_x}{\sigma_x(s)} \sqrt{1 + \frac{\mathcal{H}_x(s) \sigma_\delta^2}{\varepsilon_x}} \quad \text{and} \quad F(x) = \frac{1}{2} \int_0^1 \left[\frac{2}{u} - \ln \left(\frac{1}{u} \right) - 2 \right] e^{-x/u} du, \quad (62)$$

with c_o [m/s] speed of light, r_e [m] classical electron radius, N_e electrons in bunch, C [m] ring circumference, σ_s [m] rms. bunch length, $\sigma_{x/y}$ [m] rms beam envelopes and δ_{acc} the local momentum acceptance, i.e. the maximum momentum change for a particle from the bunch core where it is not lost. Eq. 61 applies to flat lattices only, where dispersion and emittance in the horizontal are much larger than in the vertical. Momentum acceptance is different for positive and negative momentum due to the asymmetry of the bucket, so the total loss rate is the average, i.e. $1/T = 1/2 (1/T(\delta > 0) + 1/T(\delta < 0))$.

3 The Baseline Lattice

In the following we characterize the 101 pm lattice introduced in sec. 1.5 with regard to nonlinear performance and robustness to imperfections.

3.1 Linear Optics

As mentioned in sec. 1.5 already, linear optics design was guided by the requirement for cancellation of first and second order sextupole modes by phase advance over seven cells. This is achieved by a cell tune of $[3/7, 1/7]$, which also provides a low emittance of 101 pm. Beta functions and dispersion for one super-period, i.e. one 7BA arc were shown in Fig. 1. The normalized phase advance is shown in Fig. 2.

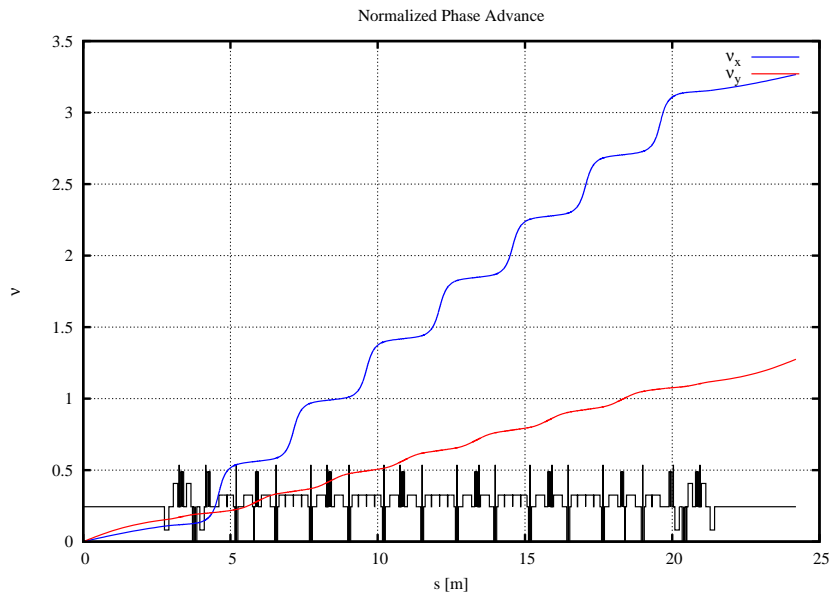


Figure 2: Normalized Phase Advance for a Super Period $\Delta\nu = [3.27, 1.27]$.

3.2 Nonlinear Optics: the Bare Lattice

Widely following the design strategy from Sec. 1.3, the nonlinear optimization was performed interactively using the OPA code: in a first step, the sextupoles were set for minimization of the five geometric 1st-order sextupole modes, in a second step the chromatic 1st-order and the 2nd-order modes were included and a steepest gradient minimizer (Powell) was used. Including ADTS and 2nd and 3rd-order chromaticities results in some distortion of the regular pattern from the first step. In particular, the chromatic sextupoles in the dispersion suppressor became rather strong, and harmonic sextupoles in the matching cells were pushed to “wrong” polarities. In a third step, ADTS and 2nd-order chromaticities and a few resonance modes were selected for linear minimization (SVD) using the octupoles. In particular h_{20020} was selected on purpose, since the systematic resonance $2\nu_x - 2\nu_y = 4 \cdot 12$ is near to the working point, and h_{31000} was selected empirically to obtain a less distorted Poincaré plot in horizontal phase space. The octupoles are considered as “trims”, i.e. the range of variation is limited, nevertheless, they are able to efficiently suppress single resonant modes and to tailor the ADTS. Of course, this process is iterative and requires empirical adjustment of weighting factors for the various terms.

Lie Generator	Effect	Normalized Value
$ k_{11001} $	$\xi_x^{(1)} \sim \partial_\delta \nu_x$	~ 0
$ k_{00111} $	$\xi_y^{(1)} \sim \partial_\delta \nu_y$	~ 0
$ h_{10002} $	$\partial_{\delta\delta} x_{\text{cod}}$	~ 0
$ h_{20001} $	$\partial_\delta \beta_x$	1.6×10^{-7}
$ h_{00201} $	$\partial_\delta \beta_y$	1.5×10^{-8}
$ h_{21000} $	ν_x	5.4×10^{-8}
$ h_{10110} $	ν_x	1.0×10^{-8}
$ h_{30000} $	$3\nu_x$	8.5×10^{-8}
$ h_{10020} $	$\nu_x - 2\nu_y$	1.5×10^{-7}
$ h_{10200} $	$\nu_x + 2\nu_y$	4.9×10^{-8}
$ h_{20110} $	$2\nu_x$	4.8×10^{-8}
$ h_{31000} $	$2\nu_x$	3.3×10^{-9}
$ h_{40000} $	$4\nu_x$	5.3×10^{-8}
$ h_{20020} $	$2\nu_x - 2\nu_y$	2.8×10^{-9}
$ h_{20200} $	$2\nu_x + 2\nu_y$	2.3×10^{-7}
$ h_{00400} $	$4\nu_y$	1.0×10^{-8}
$ h_{11200} $	$2\nu_y$	3.3×10^{-8}
$ h_{00310} $	$2\nu_y$	3.9×10^{-8}

Lie Generator	Effect	Normalized Value
$ k_{22000} $	$\partial_{J_x} \nu_x$	3.6×10^{-7}
$ k_{11110} $	$\partial_{J_y} \nu_x, \partial_{J_x} \nu_y$	5.9×10^{-8}
$ k_{00220} $	$\partial_{J_y} \nu_y$	8.1×10^{-8}
$ k_{22001} $	$\partial_{J_x} \delta \nu_x$	3.3×10^{-7}
$ k_{11111} $	$\partial_{J_y} \delta \nu_x, \partial_{J_x} \delta \nu_y$	7.8×10^{-7}
$ k_{00221} $	$\partial_{J_y} \delta \nu_y$	5.9×10^{-8}
$ k_{11002} $	$\xi_x^{(2)} \sim \partial_{\delta\delta} \nu_x$	4.0×10^{-7}
$ k_{00112} $	$\xi_y^{(2)} \sim \partial_{\delta\delta} \nu_y$	1.3×10^{-7}
$ k_{11003} $	$\xi_x^{(3)} \sim \partial_{\delta\delta\delta} \nu_x$	5.7×10^{-8}
$ k_{00113} $	$\xi_y^{(3)} \sim \partial_{\delta\delta\delta} \nu_y$	2.7×10^{-8}
$ k_{33000} $	$\partial_{J_x J_x} \nu_x$	5.1×10^{-8}
$ k_{22110} $	$\partial_{J_x J_y} \nu_x, \partial_{J_x J_x} \nu_y$	9.3×10^{-8}
$ k_{11220} $	$\partial_{J_y J_y} \nu_x, \partial_{J_x J_y} \nu_y$	2.0×10^{-7}
$ k_{00330} $	$\partial_{J_y J_y} \nu_y$	4.5×10^{-8}

Table 4: Normalized Magnitude of the Lie Generators.

The lattice then was analyzed to arbitrary order based on TPSA calculations. Table 4 displays the normalized magnitude of the Lie generators.

The following figures visualize the nonlinear performance for the bare (i.e. error-free) lattice:

Fig. 3 shows the bucket at a voltage of 1.4 MV of the 500 MHz RF-system. Due to a relatively large second order momentum factor of $\alpha_2 = 1.05 \cdot 10^{-3}$ (about 8 times larger than α_1) the bucket is quite asymmetric along the energy axis, i.e. a particle starting at moderate negative momentum reaches rather large positive momentum values. At higher voltage the bucket becomes a so-called alpha bucket where the two buckets contain elliptic and hyperbolic fix point pairs at same phase, whereas for lower voltage they contain the fix point pairs at same energy. Transition occurs at 1.99 MV.

Fig. 4 shows the dynamic aperture on-momentum and for $\pm 5\%$ momentum deviation. Tracking was done in 6-D including synchrotron oscillations for 1.8 MV cavity voltage. The dynamic aperture for particles starting at -5% is relatively small, because these particles reach quite large positive momenta due to the bucket asymmetry.

Fig. 5: upper plots shows the tunes as function of initial betatron amplitudes at the middle of straight, as it is relevant for injection. Tracking results and the predictions from perturbation theory (up to 8th order in phase space coordinates) are displayed, indicating that the higher order contributions are still moderate near the aperture limit. The lower plot shows the chromaticities: the linear part has been corrected to zero, and the residual higher orders determine the tune footprint.

Fig. 6: the upper plot shows the the on-momentum tune footprint in the tune diagram. The tune has been placed to avoid overlap with non-systematic low order sextupole resonances which get activated in the real lattice where engineering tolerances perturb the periodicity. Note that the *systematic* 4th-order resonance $2\nu_x - 2\nu_y = 4 \cdot 12$ is ‘hiding’ behind the main coupling resonance, but its driver h_{20020} was deliberately suppressed with the octupoles (see corresponding entry in Table 4. The lower plot shows

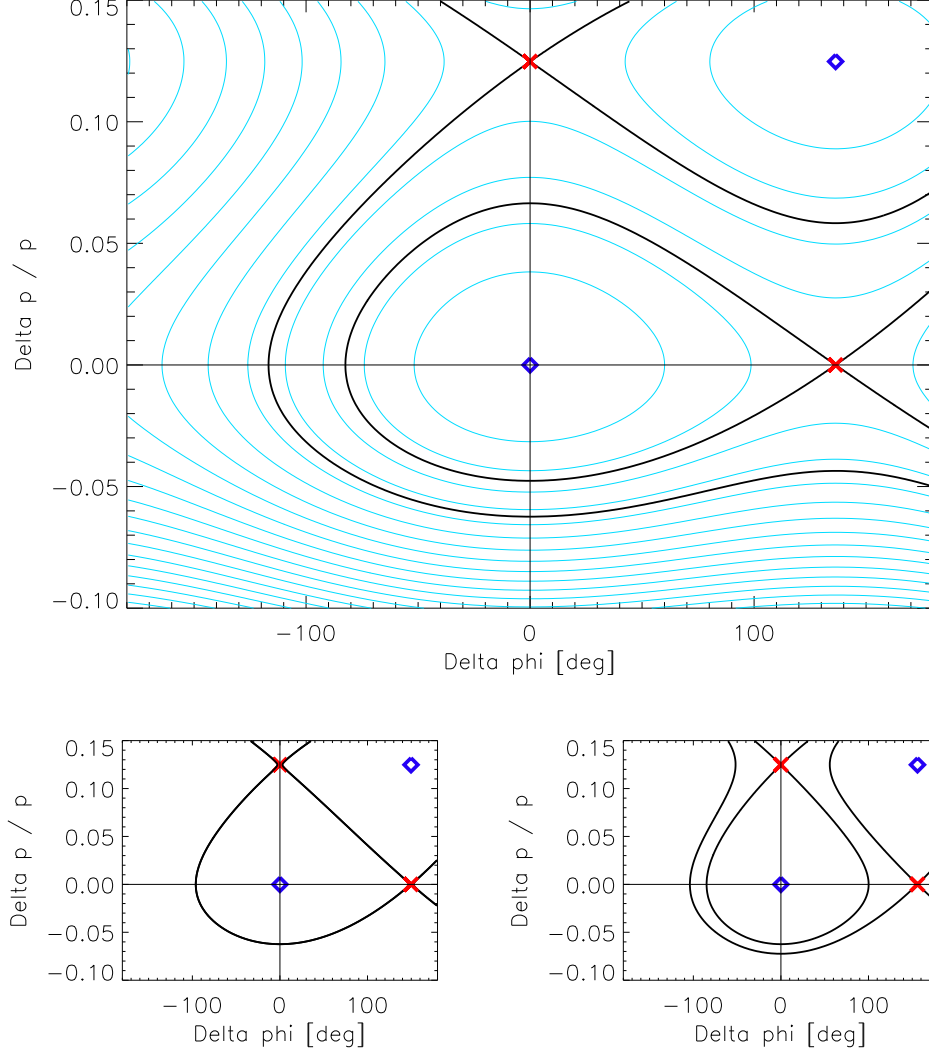


Figure 3: Longitudinal Dynamics: top plot shows the bucket for 1.4 MV voltage at 500 MHz RF. The small plots show the bucket for 1.99 MV and 2.4 MV voltage. Elliptic and hyperbolic fix points are marked by blue diamonds and red crosses. Separatrices are shown as thick lines.

the frequency map in real space indicating that there are no strong resonances.

Fig. 7: upper plot shows the off-momentum tune footprint in the tune diagram and the lower plot shows the frequency map in momentum and horizontal real space. Calculations were done for fixed momentum otherwise chromatic tune variation due to synchrotron oscillations would cover up any tune shift due to diffusion.

Fig. 8 shows the momentum acceptance obtained from Touschek tracking, i.e. starting particles at the bunch core with an energy offset and binary search for maximum offset where particles are not lost. Following parameters were assumed: Emittances $\varepsilon_x = 101$ pm-rad (IBS neglected), $\varepsilon_y = 10$ pm-rad, bunch charge $Q_b = 0.994$ nC, i.e. beam current $I_b = 400$ mA in 390 of $h_{RF} = 484$ buckets, circumference $C = 290.4$ m, bunch length $\sigma_s = 2.58$ mm, energy spread $\sigma_\delta = 0.103\%$. The resulting life time is $\tau = 4.6$ hrs, which would give about 4 hrs taking into account residual gas scattering. Including IBS and a harmonic cavity to stretch the bunches by a factor 2–3, a total lifetime of more than 10 hrs may be expected which fulfills the requirements.

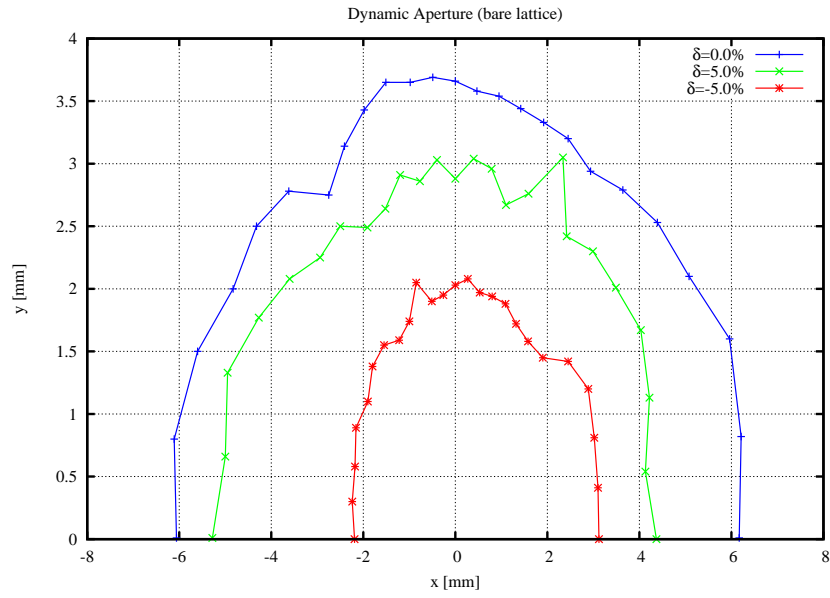


Figure 4: On and Off-Momentum Dynamic Aperture for Bare Lattice (2,064 turns; with RF cavity).

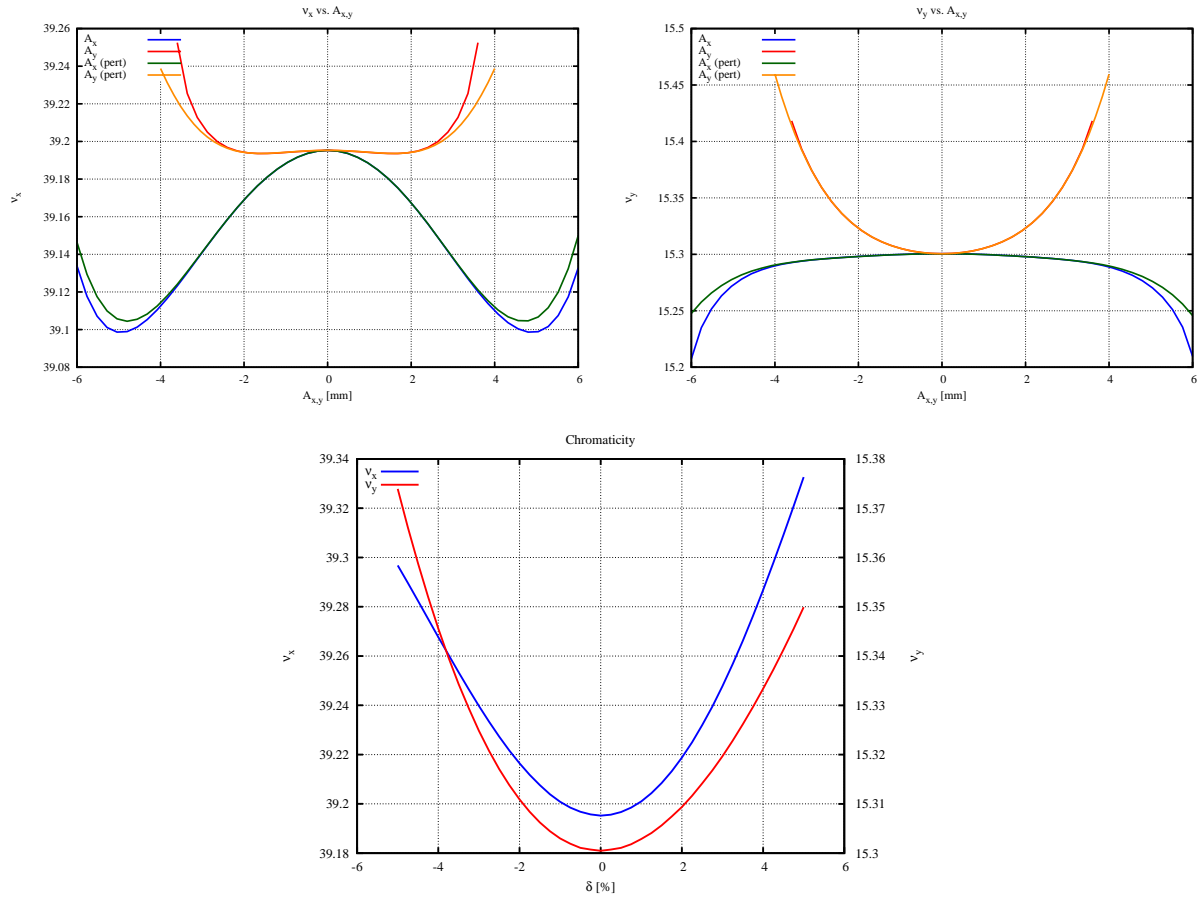


Figure 5: ADTS and chromaticity: top plots show horizontal (left) and vertical (right) tune as a function of horizontal and vertical amplitude, also showing the predictions from 2nd-order perturbation theory. Bottom plot shows the chromaticities, i.e. the tunes as a function of momentum.

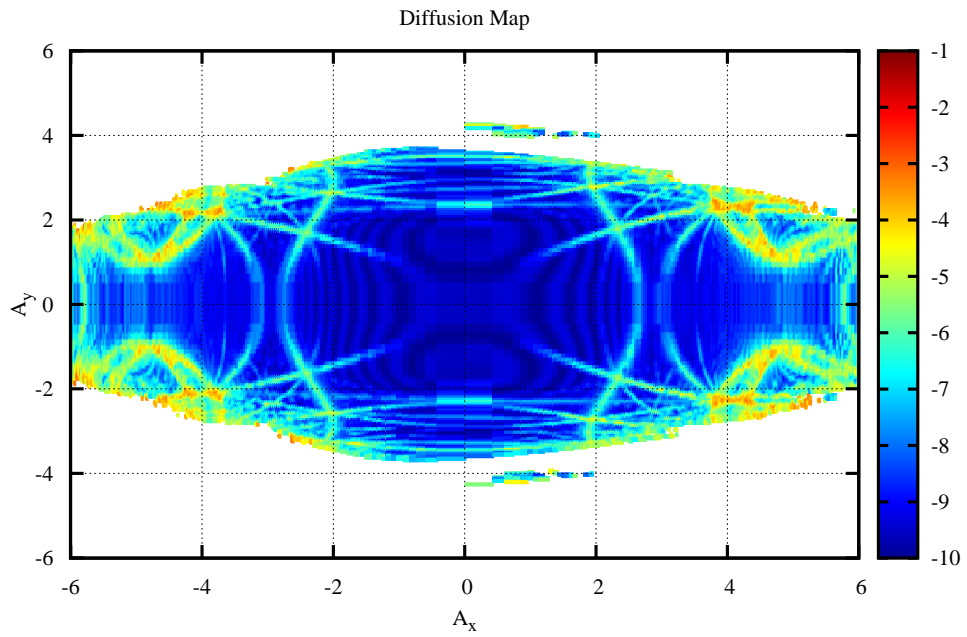
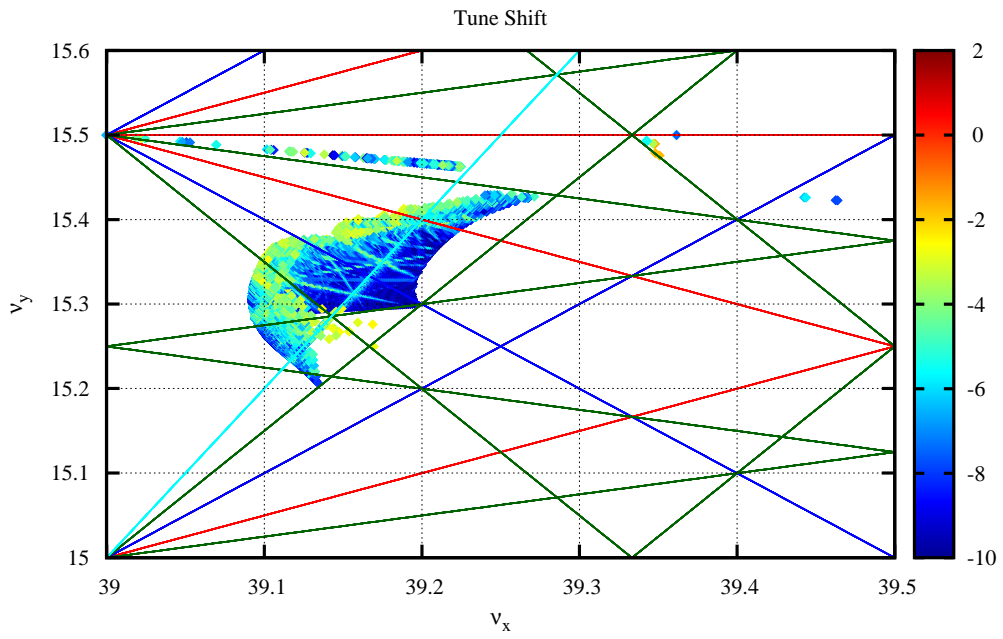


Figure 6: On-Momentum Frequency Map for Bare Lattice (4,128 turns).

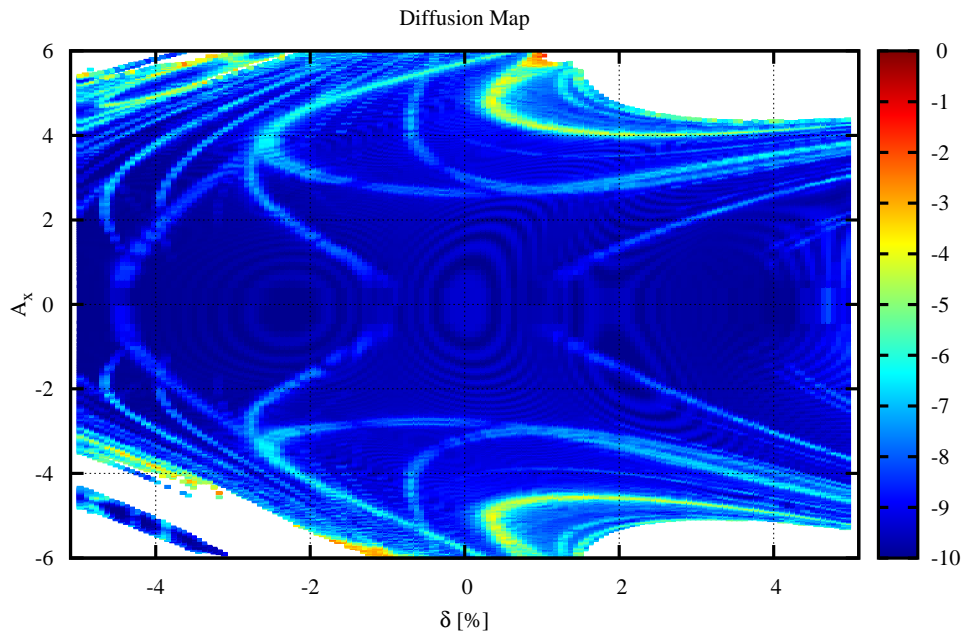
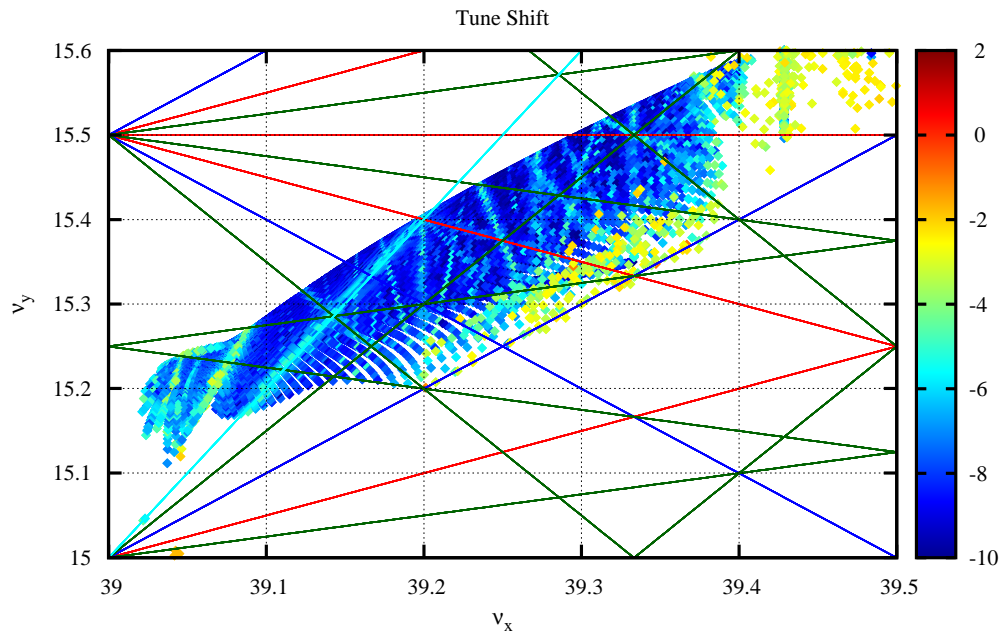


Figure 7: Off-Momentum Frequency Map for Bare Lattice (4,128 turns).

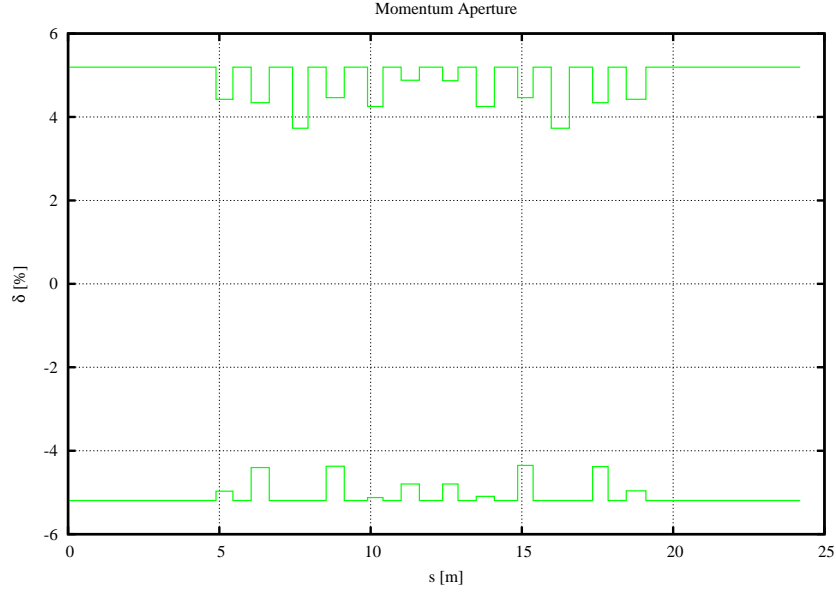


Figure 8: Touschek Tracking Bare Lattice.

3.3 Real Lattice

Engineering tolerances according to Sec. B were applied to all elements. So far no correlations between elements have been considered, which might improve the results.

144 BPMs and horizontal/vertical correctors were used for orbit correction. The correctors were assumed to be realized as additional coils in sextupoles, as it was done at SLS. Fig. 9 shows the residual rms orbit after correction proving the robustness of orbit correction: The orbit is corrected to zero at the BPMs. The excursion between is plotted as a bar at each element. The bar is centered at the average orbit, which is non-zero due to the limited number of seeds, and the size of the bar is given by the rms orbit from all seeds. Since the orbit is well corrected, the rms value is comparable to the mean value.

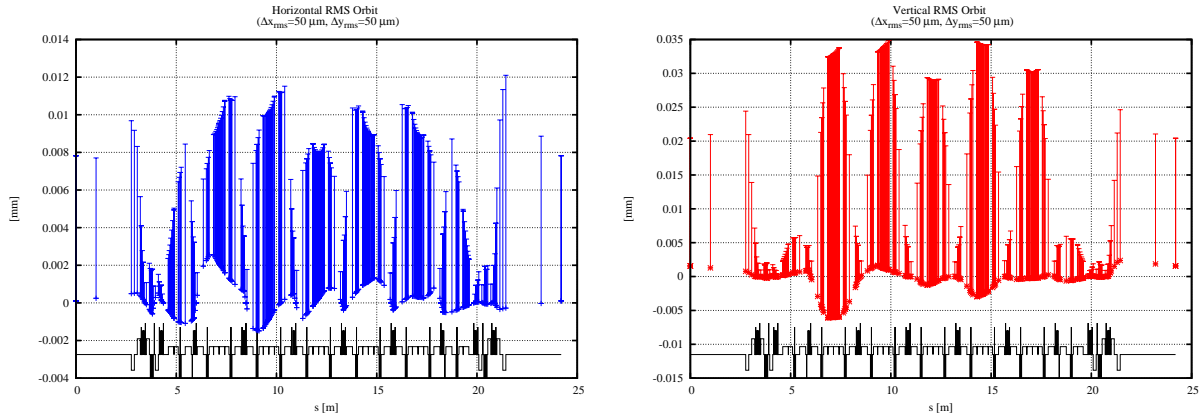


Figure 9: Robust Control of Orbit.: horizontal (top) and vertical (bottom) orbit after correction. Minima and maxima of the bars are given by $\langle x \rangle \pm \sqrt{\langle x^2 \rangle}$.

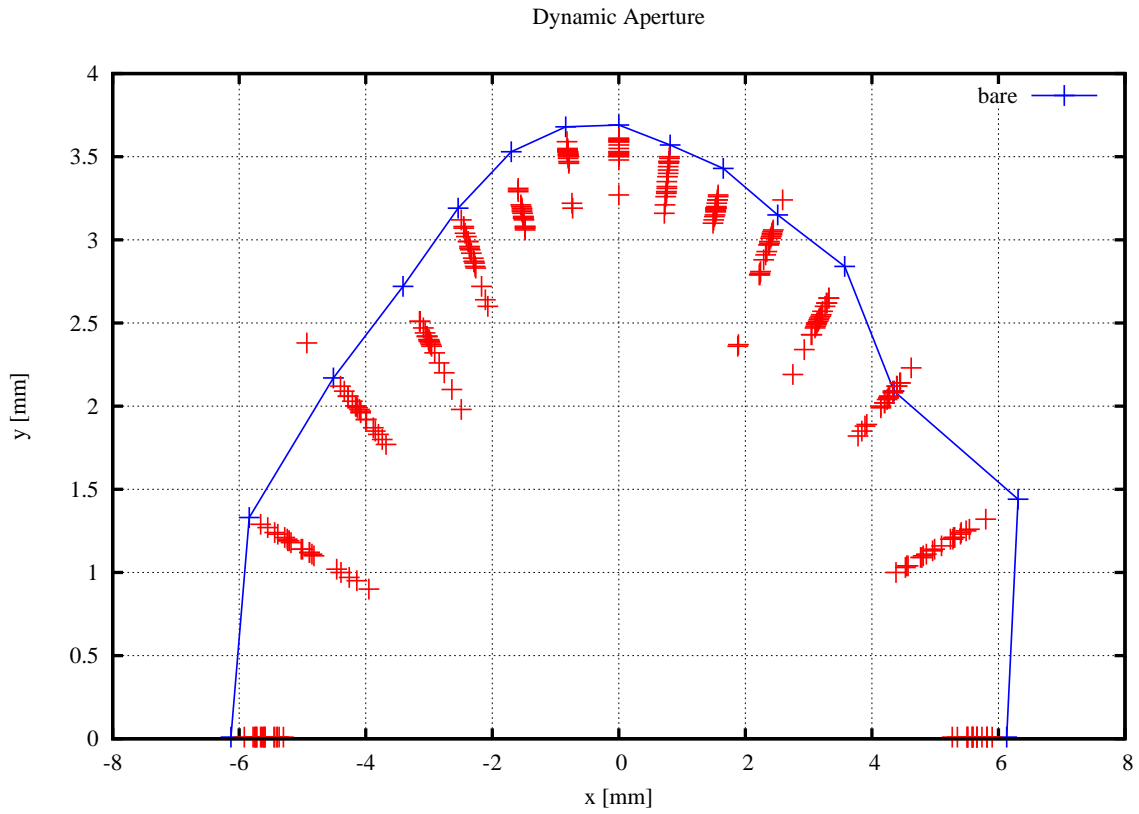


Figure 10: Dynamic Aperture for Bare and Real Lattice (4096 turns).

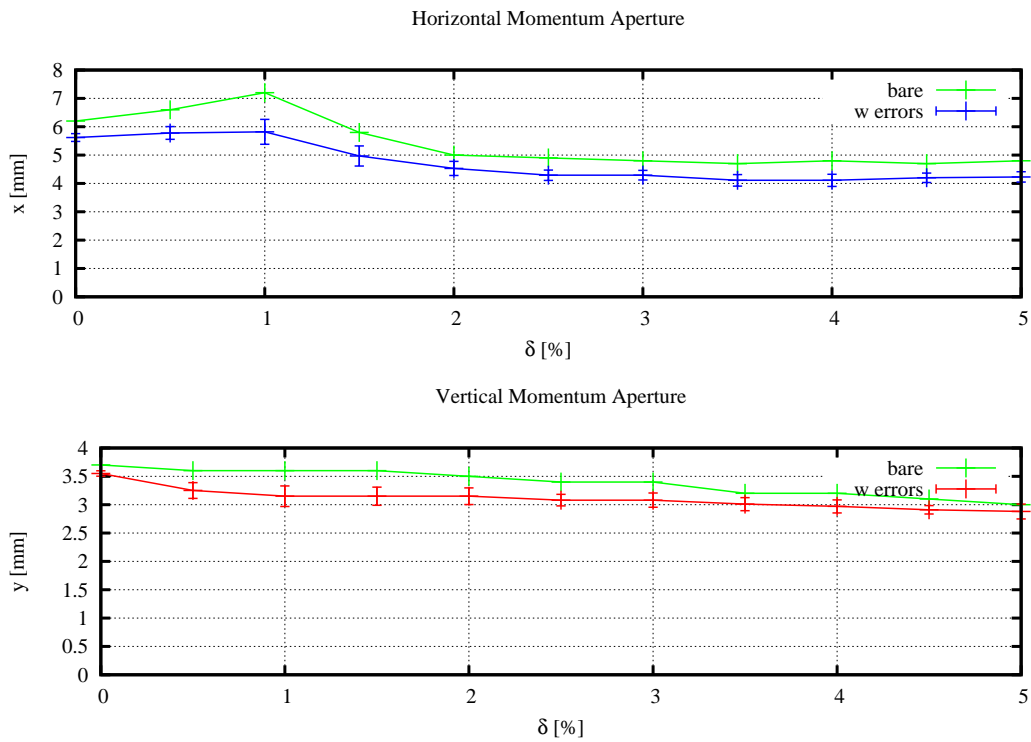


Figure 11: Off-Momentum Dynamic Aperture for Bare and Real Lattice (4096 turns).

Fig. 10 shows the degradation of the bare lattice on-momentum dynamic aperture due to engineering tolerances for various seeds. Still, a horizontal aperture of more than $\pm 5\%$ is left thus supporting confidence in feasibility of off-axis injection.

Fig. 11 shows the horizontal and vertical dynamic aperture as a function of momentum with and without engineering tolerances. This is in particular important for Touschek lifetime since particles from the bunch core which gain or lose energy due to inelastic scattering start horizontal betatron oscillations around the corresponding off-momentum orbits.

Fig. 12 show the tune footprint as function of initial betatron amplitudes and the frequency map in real space with engineering tolerances and should be compared to 6: the web of resonance lines is much more dense due to activation of non-systematic resonances, however the deterioration is moderate.

Fig. 13 shows the tune footprint as function of momentum and the frequency map in momentum and horizontal coordinate as should be compared to 7. Now trapping by higher order resonances becomes visible, but, again, the deterioration is moderate.

Fig. 14 shows the momentum acceptance obtained from Touschek tracking for one particular error seed and for the complete lattice. There is virtually no degradation compared to Fig. 8 for one achromat of the bare lattice: due to the relatively low RF voltage of 1.4 MV, the lattice momentum acceptance is smaller than the RF momentum acceptance and thus degradation due to engineering tolerances has little impact.

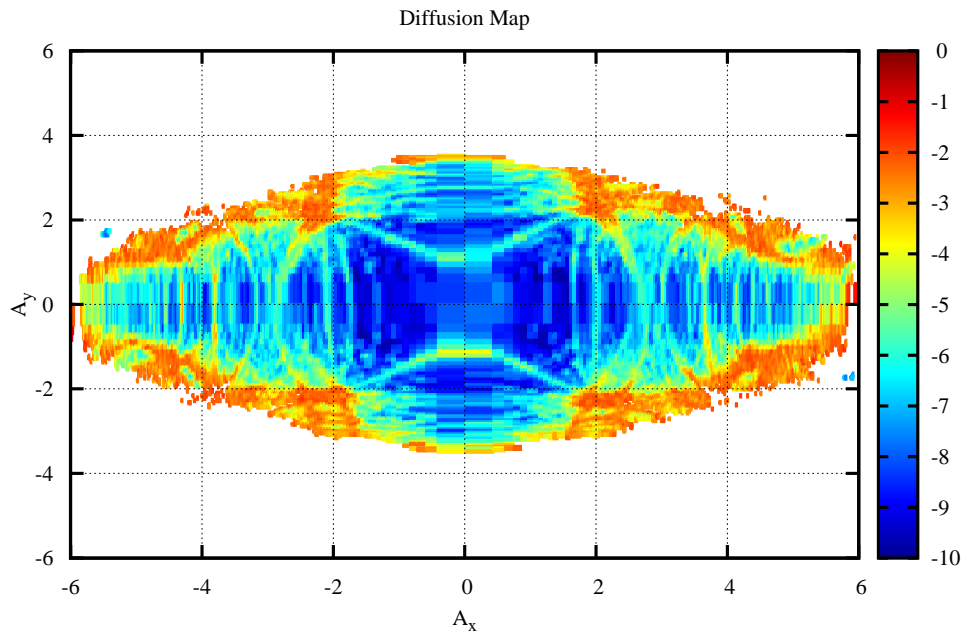
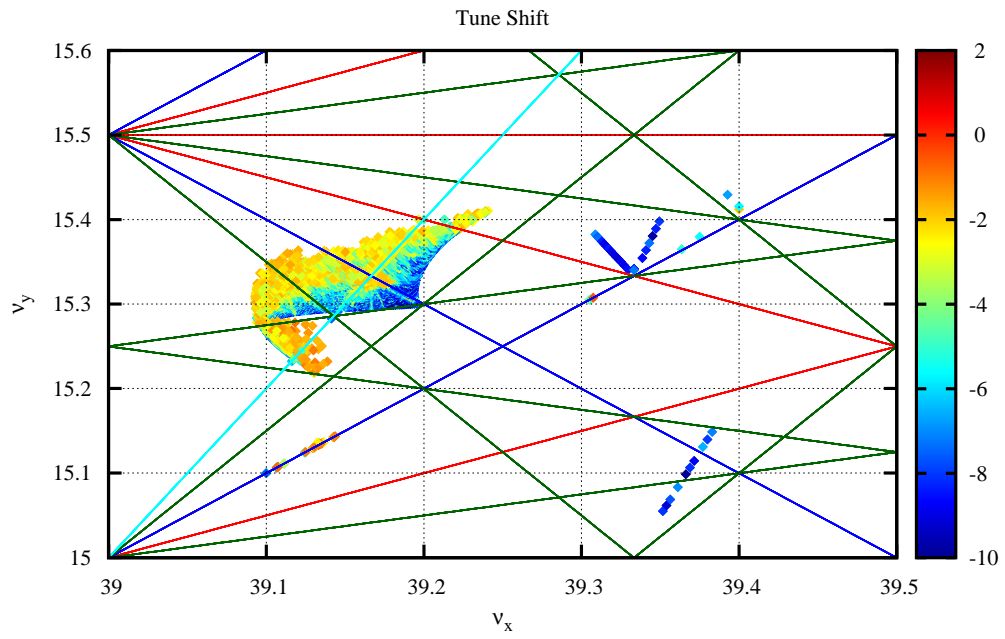


Figure 12: On-Momentum Frequency Map for Real Lattice (4,128 turns).

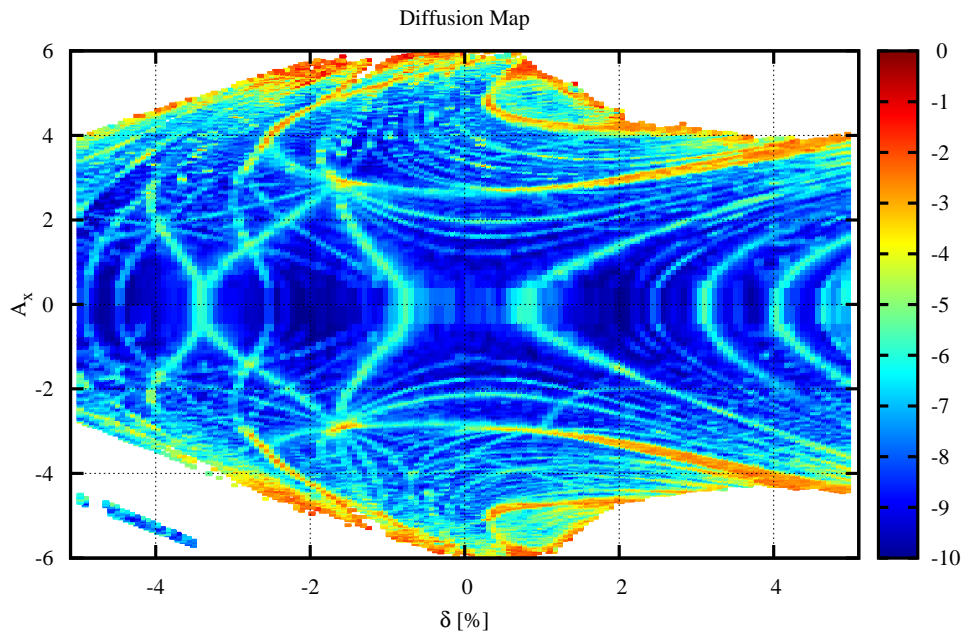
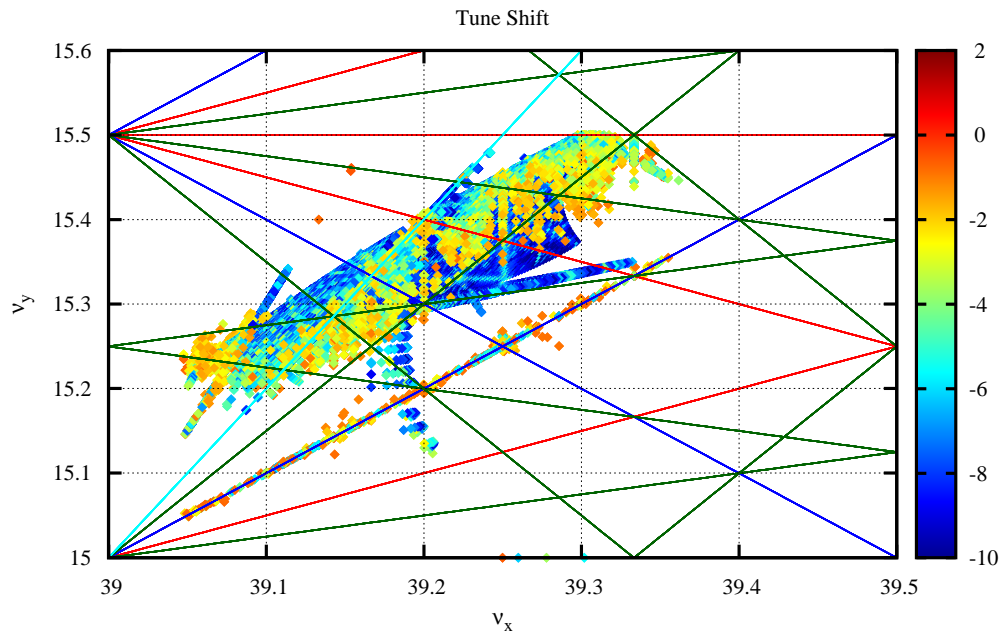


Figure 13: Off-Momentum Frequency Map for Real Lattice (4,128 turns).

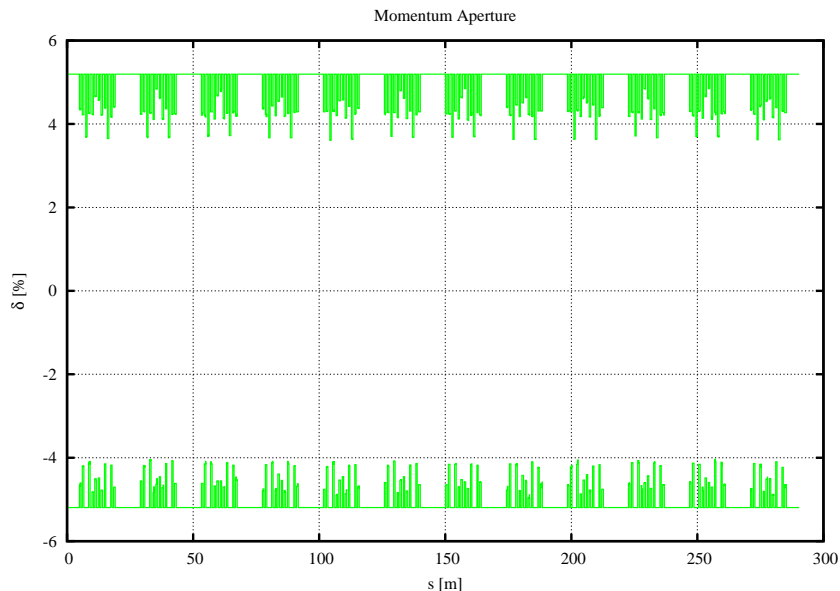


Figure 14: Touschek Tracking Real Lattice.

4 Conclusions and Outlook

A robust design strategy has been established and applied to SLS-2. For a low emittance ring with strong non-linearities suppression of the Hamiltonian modes of first order in sextupole strength and of second order in sextupole, resp. first order in octupole strength via phase cancellations is essential and affects the linear lattice design strongly. Perturbative violation of the cancellation scheme in order to manipulate single phase independent or resonant terms leads to a further improvement of dynamic acceptances.

The present so called CDR-reference lattice revealed a weak point since one second order mode was amplified coherently: dynamic apertures, although large for the bare lattice, deteriorated much when engineering tolerances were applied. A robust solution was found for a complete cancellation based on a lattice cell with even stronger focusing, which, as a pleasant side-effect, significantly further reduced the emittance. However, the lattice study presented here is not yet feasible with regard to space constraints but gives a high level of confidence that a design is within reach.

Combining the non-linear optics optimization strategy with technical constraints will be the next step in order to arrive at a feasible, robust lattice, which then will become the new reference. From the engineering point of view, the modifications will appear small and the parameters of the component will change only in a few percent range, thus no engineering design work based on the present reference is wasted.

Further studies will investigate and design an optics for non-zero chromaticity, as may be required for suppression of coupled bunch instabilities, implement correlated misalignment errors modelling the girder/magnet hierarchy, design off-axis and on-axis injections schemes, and explore the option for a round beam based on a “Moebius” lattice as outlined in appendix C.

Acknowledgement

We would like to thank Masamitsu Aiba for performing cross-checks using other codes, Michael Böge for his help with installation of Tracy 3.5, and both for many useful discussions. We would also like to thank Jan Chrin for some insightful discussions regarding accelerator control and on-line modeling, and, in particular, for his swiftly prototyped Python interface for Tracy-2,3; by using Cython [41].

References

- [1] C. Gough, M. Aiba “Top-Up Injection with Anti-Septum” IPAC 2017.
- [2] M. Eriksson, L.-J. Lindgren, M. Sjöström, E. Wallén, L. Rivkin, A. Streun, “Some Small-Emittance Light-Source Lattices with Multi-Bend Achromats”, NIM A 587, 221-226 (2008).
- [3] A. Streun, M. Aiba, M. Böge, M. P. Ehrlichman, Á Saá Hernández, and H. Xu, “Upgrade of the Swiss Light Source Storage Ring based on a Lattice combining Longitudinal Gradient Bends and Anti-Bends”, ICFA Beam Dynamics Newsletter No.70, 2017.
- [4] A. Streun, M. Aiba, M. Böge, C. Calzolaio, M. Ehrlichman, A. Müller, Á. Saá Hernández, H. Xu “Proposed Upgrade of the SLS Storage Ring” IPAC 2016.
- [5] A. Streun “SLS-2 Upgrade of the Swiss Light Source” 2nd Low Emittance Rings Workshop 2016.
- [6] A. Streun, M. Aiba, M. Böge, M. Ehrlichman “Design Studies for an Upgrade of the SLS Storage Ring” IPAC 2015.
- [7] A. Wrulich “Overview of 3rd Generation Light Sources” Workshop on Fourth Generation Light Sources, SSRL/SLAC, Stanford, CA, 1992.
- [8] A. Streun, A. Wrulich “Compact Low Emittance Light Sources Based on Longitudinal Gradient Bending Magnets” NIM 770, 98-112 (2015).
- [9] J.P. Delahaye, J.P. Potier “Reverse Bending Magnets in a Combined Function Lattice for the CLIC Damping Ring” PAC 1989.
- [10] A. Streun “The anti-bend cell for ultralow emittance storage ring lattices” NIM 737, 148-154 (2014).
- [11] S.C. Leemann “The MAX IV 3 GeV Storage Ring” ICFA Newsletter 57, 25-35 (2012).
- [12] S.C. Leemann, A. Streun “Perspectives for Future Light Source Lattices Incorporating Yet Uncommon Magnets” PR ST-AB 14 030701 (2011).
- [13] MAX IV DDR 2010.
- [14] S.C. Leemann, Å. Andersson, M. Eriksson, L.-J. Lindgren, E. Wallén, J. Bengtsson, A. Streun “Beam dynamics and Expected Performance of Sweden’s New Storage-ring Light Source: MAX IV” PR ST-AB 12, 120701 (2009).
- [15] J. Bengtsson “The Sextupole Scheme for the Swiss Light Source (SLS): An Analytic Approach” SLS 9/97 (1997).
- [16] M.P. Ehrlichman, “Genetic Algorithm for Chromaticity Correction in Diffraction Limited Storage Rings” PR ST-AB 19, 044001 (2016).

- [17] M.P. Ehrlichman, M. Aiba, A. Streun “Optimizaing SLS-2 Nonlinearities Using a Multi-Objective Genetic Optimizer” IPAC 2015.
- [18] J.D. Jackson “From Lorenz to Coulomb and Other Explicit Gauge Transformations” LBNL-50079 (2002).
- [19] J. Bengtsson “Non-Linear Transverse Dynamics for Storage Rings with Applications to the Low-Energy Antiproton Ring (LEAR) at CERN” CERN 88-05.
- [20] W. Gröbner “Die Lie-Reihen und ihre Anwendungen” (Deutscher Verlag der Wissenschaften, Berlin 1960).
- [21] E.D. Courant, H.S. Snyder “Theory of the Alternating-Gradient Synchrotron” Ann. Phys. 3, 1-48 (1958).
- [22] H. Yoshida “Construction of Higher Order Symplectic Integrators” Phys. Lett. A 150, 262-268 (1990).
- [23] E.Forest, R.D. Ruth “Fourth-Order Symplectic Integration” Physica D 42, 105-117 (1990).
- [24] F. Neri “Lie Algebras and Canonical Integration” Unpubl. Univ. of Maryland (1987).
- [25] M. Sands “The Physics of Electron Storage Rings” SLAC-121 (1970).
- [26] J.M. Finn “Lie Transforms: A Perspective” Local and Global Methods of nonlinear Dynamics ,Lecture Notes in Physics 252, 63-86 (1984).
- [27] A.J. Dragt, J.M. Finn “Lie Series and Invariant Functions for Analytic Symplectic Maps” J. Math. Phys. 17, 2215-2227 (1976).
- [28] E. Forest “A Hamiltonian-Free Description of Single Particle Dynamics for Hopelessly Complex Periodic Systems” J. Math. Phys. 31(5), 1133-1144 (1990).
- [29] J. Bengtsson, J. Irwin “Analytical Calculations of Smear and Tune Shift” SSC-232 (1990).
- [30] A. Bazzani, P. Mazzanti, G. Servizi, G. Turchetti “Normal Forms for Hamiltonian Maps and Nonlinear Effects in a Particle Accelerator” Nuovo Cimento B 102, 51-80 (1988).
- [31] A. Streun et al “Commissioning of the Swiss Light Source” PAC 2001.
- [32] ados.web.psi.ch/opa.
- [33] J. Bengtsson “NSLS-II: Control of Dynamic Aperture” BNL-81770-2008-IR (2008).
- [34] J. Laskar “Frequency Map Analysis and Particle Accelerators” PAC 2003.
- [35] V.I. Arnold “Proof of a theorem of A.N. Kolmogorov on the Preservation of Conditionally Periodic Motions Under a Small Perturbation of the Hamiltonian” Uspehi Mat. Nauk 18 (1963).
- [36] J. Moser, “On Invariant Curves of Area-Preserving Mappings of an Annulus” Nachr. Akad. Wiss. Göttingen, II, 1–20 (1962).
- [37] A.N. Kolmogorov “On the Conservation of Conditionally Periodic Motions under Small Perturbation of the Hamiltonian” Dokl. Akad. Nauk SSR 98, 525-530 (1954); Engl. Transl. LNP 93, 51-56 (1979).
- [38] A. Streun “Momentum Acceptance and Touschek Lifetime” SLS Note 18/97 (1997).

- [39] J. Le Duff “Single and Multiple Touschek Effects” p. 114-130 CERN 89-01 (1989).
- [40] C. Bernardini, G.F. Corazza, G. Di Giugno, G. Ghigo, J. Haissinski, P. Marin, R. Querzoli, B. Touschek “Lifetime and Beam Size in a Storage Ring” Phys. Rev. Lett. 10, 407-409 (1963).
- [41] J. Chrin “A Cython Interface to EPICS Channel Access for High-Level Python Applications” PCaPAC 2016.
- [42] E.I. Antokhin et al. “Multipoles of the SLS Storage Ring: Manufacturing and Magnetic Measurements” IEEE Trans. Appl. Supercond. 12, 51-54 (2002).
- [43] E.I. Antokhin et al “Precise Magnetic Measurements of the SLS Storage Ring Multipoles: Measuring System and Results” PAC 2001.
- [44] V. Vrankovic, D.C. George “Smooth Shimming of Pole Profiles” IEEE Trans. Appl. Supercond. 10, 1372-1375 (2000).
- [45] A. Streun “Simulations for SLS Storage Ring Dynamic Aperture with Measured Magnet Multipole Errors” SLS-TME-TA-1999-0012 (1999).
- [46] S. Henderson, M. Billing, R. Holtzapple, R. Littauer, B. McDaniel, D. Rice, D. Rubin, D. Sagan, R. Talman, A. Temnykh “Investigation of the Mobius Accelerator at CESR” PAC 1999.
- [47] M. Aiba, M. Ehrlichman, and A. Streun “Round Beam Operation in Electron Storage Rings and Generalisation of Moebius Accelerator” IPAC 2015.
- [48] J. Bengtsson, I. Pinayev “NSLS-II: Control of Vertical Beam Size” NSLS-II Tech Note (2007).
- [49] C. Steier, D. Robin, A. Wolski, G. Portmann, J. Safranek “Coupling Correction and Beam Dynamics at Ultralow Emittance in the ALS” PAC 2003.
- [50] J.-P. Delahaye, J. Jäger “Variation of the Dispersion Function, Momentum Compaction Factor, and Damping Partition Numbers with Particle Energy Deviation” Part. Accel., 183-201, (1986).
- [51] D. Robin, E. Forest, C. Pellegrini, A. Amiry, “Quasi-Isochronous Storage Rings” Phys. Rev. E 48 , 2149-2156 (1993).

A Reference Lattice Benchmarks

For a comparison, the benchmarks used for the here presented robust approach and solution have also been applied to the 139 pm emittance lattice, which still is the reference for the conceptual design report, but will be abandoned as soon as a version of the new 101 pm lattice will have been established, which is feasible with regard to inter-magnet distances etc.

Figures 15–22 corresponding to Figs. 4–13 of the new baseline lattice.

For the reference lattice, the dynamic aperture according to Fig. 15 looks reasonable, but Figs. 16 (top), 17 (top) and 18 (top) reveal that the rather larger ADTS leads to a crossing of the systematic 5th-order resonance $3\nu_x + 2\nu_y = 11 \cdot 12$, causing an increase of vertical oscillation amplitude and potential particle loss at narrow gaps.

This resonance is driven by cross terms from the earlier mentioned $2\nu_x + 2\nu_y$ and ν_x , the latter a leading order sextupolar resonance. Besides, an evaluation of the driving terms to 5th order (in the phase-space coordinates) reveals that there are quite a few rather strong cross terms.

Furthermore, the resonance crossing occurs at $x \approx \pm 3$ mm, just where the vertical ADTS exhibits a “folding” and is most vulnerable. This leads to the collapse of the on and off-momentum dynamic aperture when engineering tolerances are included.

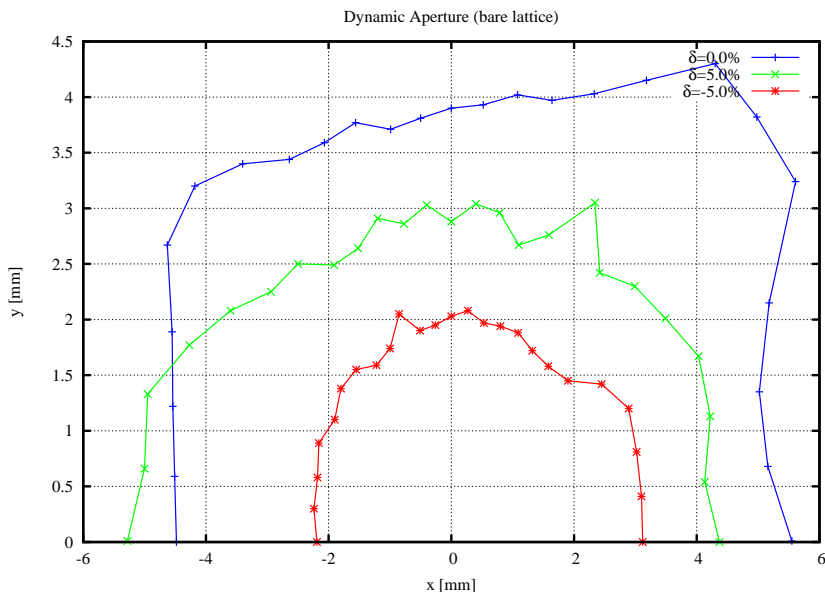


Figure 15: On and Off-Momentum Dynamic Aperture for Bare Lattice (2,064 turns; with RF cavity).

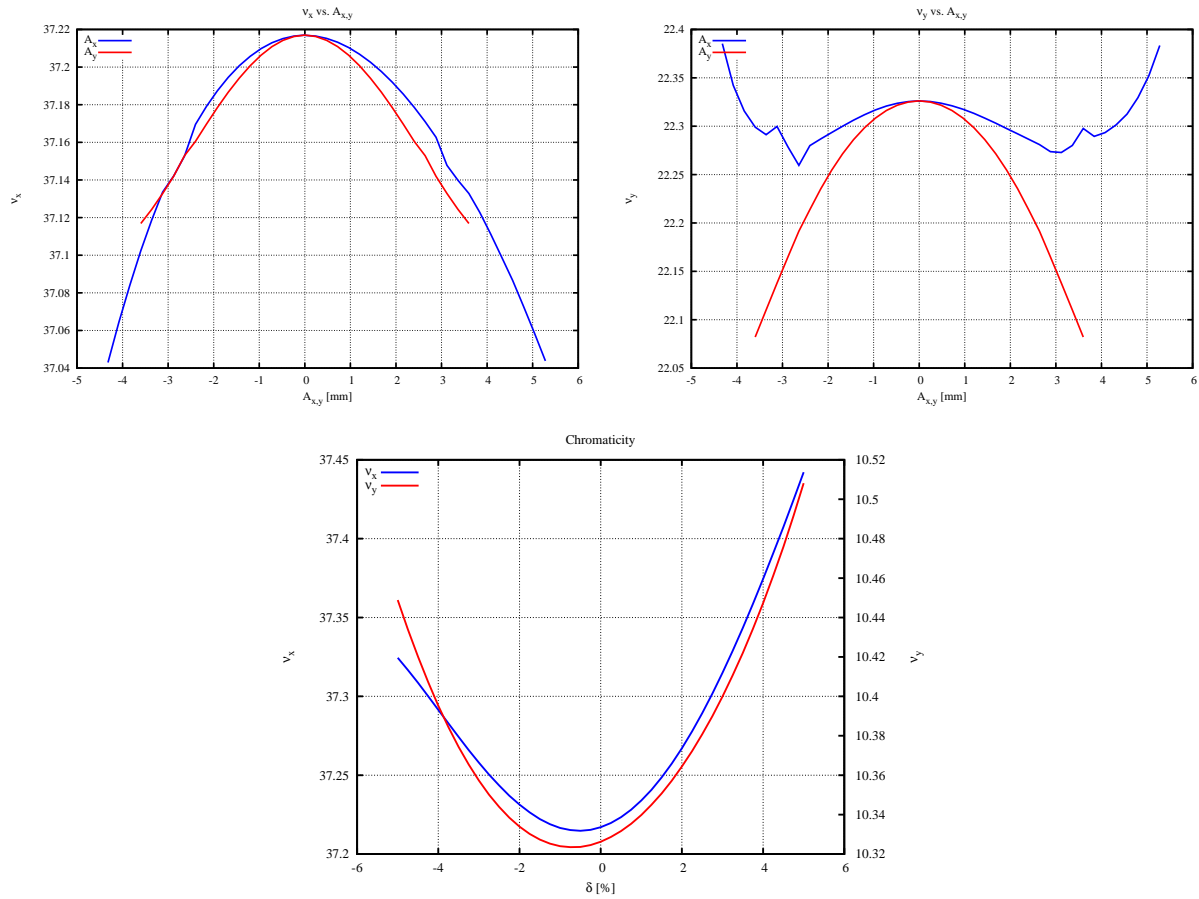


Figure 16: ADTS and chromaticity: Top plots show horizontal (left) and vertical (right) tune a function of horizontal and vertical amplitude. Bottom plot shows the chromaticities, i.e. the tunes as a function of momentum.

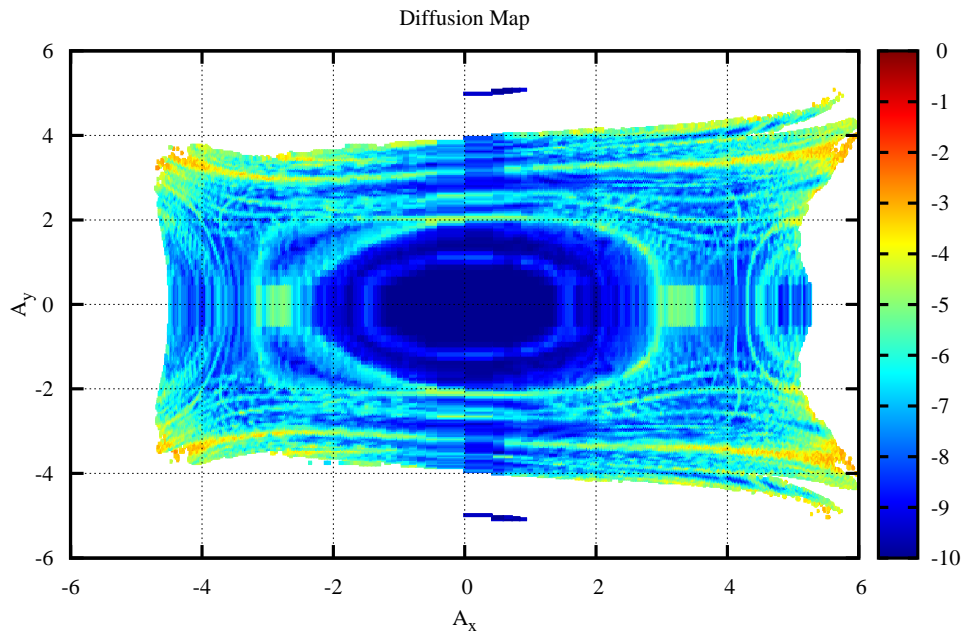
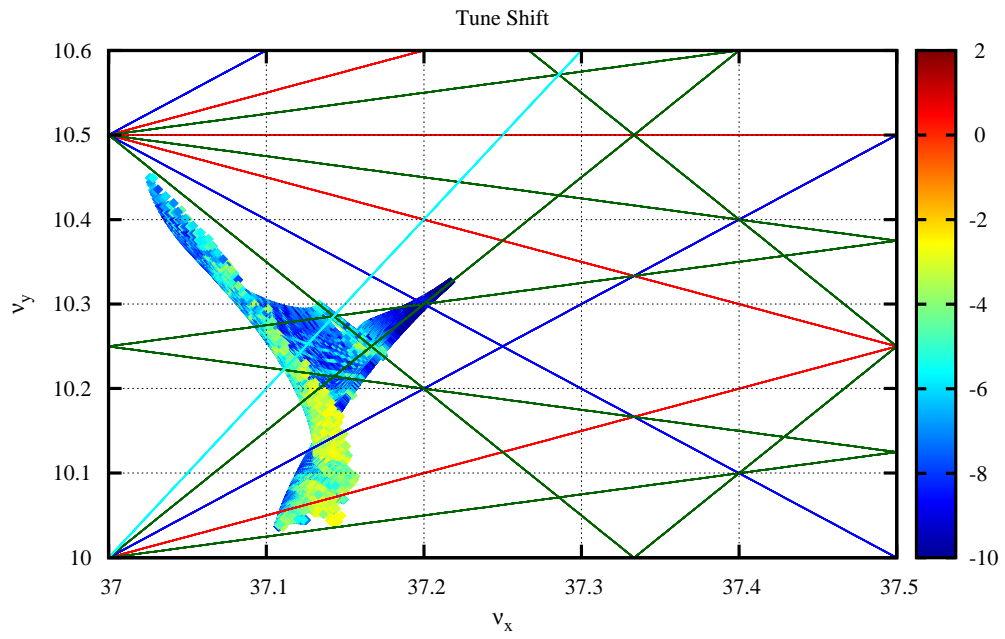


Figure 17: On-Momentum Frequency Map for Bare Lattice (4,128 turns).

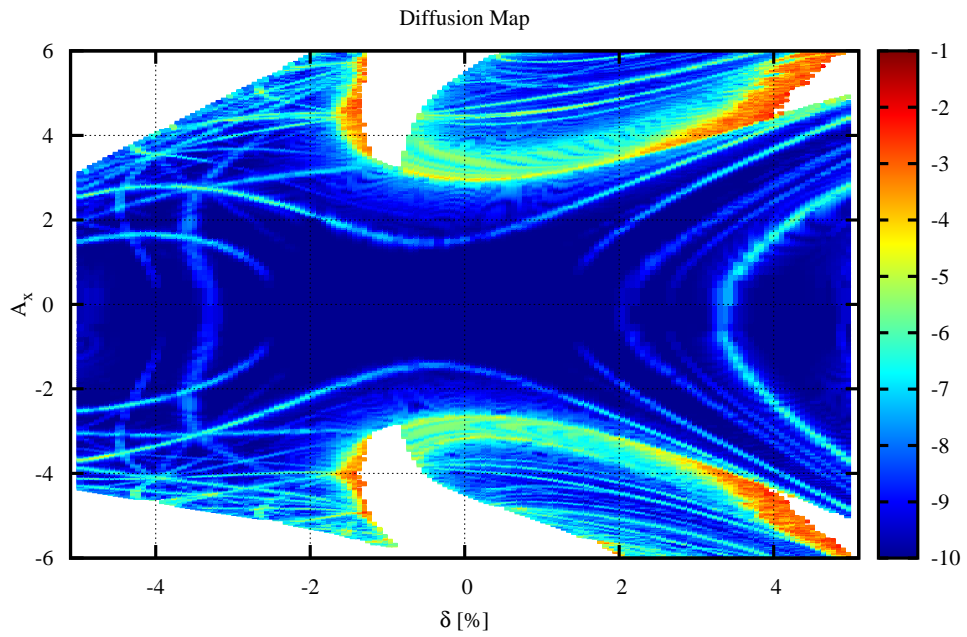
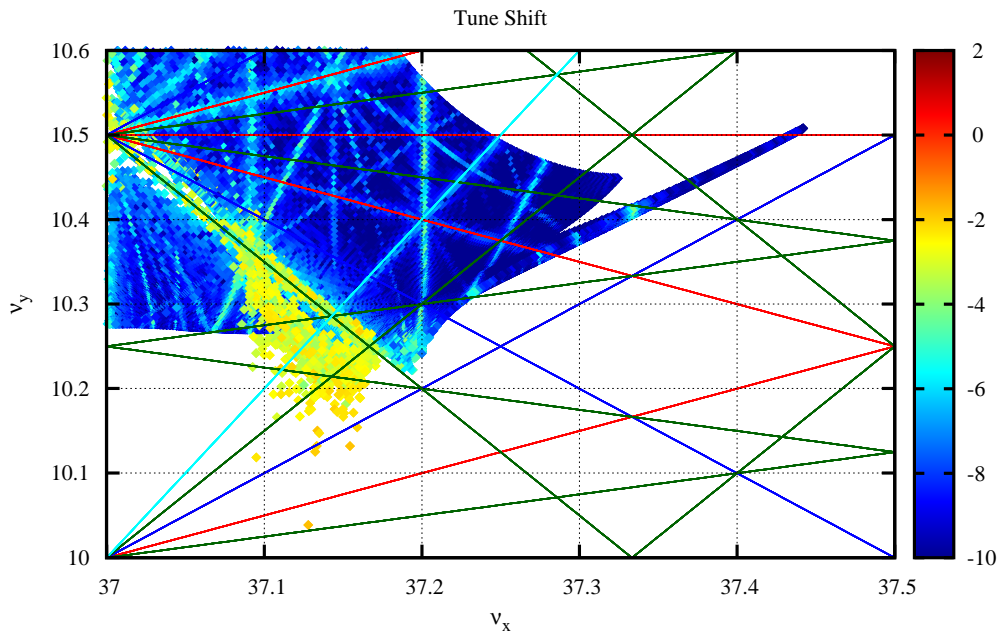


Figure 18: Off-Momentum Frequency Map for Bare Lattice (4,128 turns).

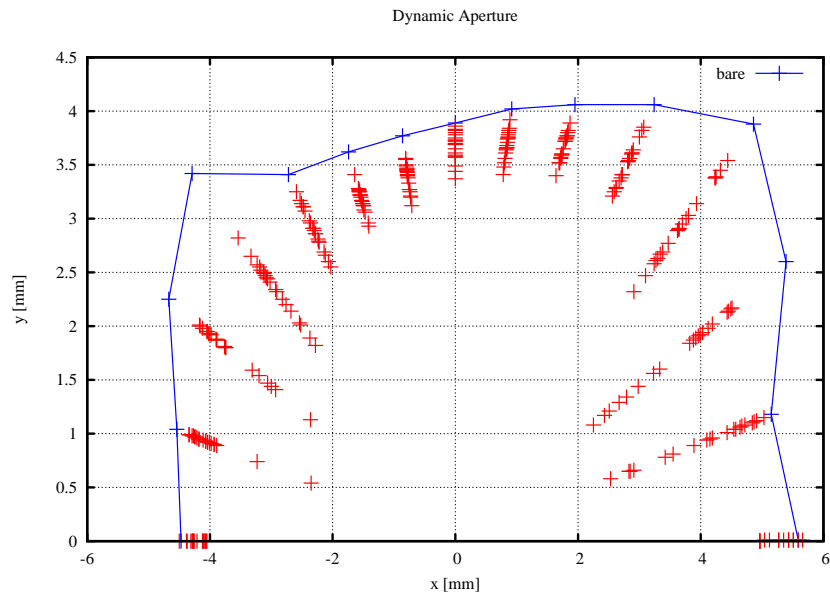


Figure 19: Dynamic Aperture for Bare and Real Lattice (4096 turns).

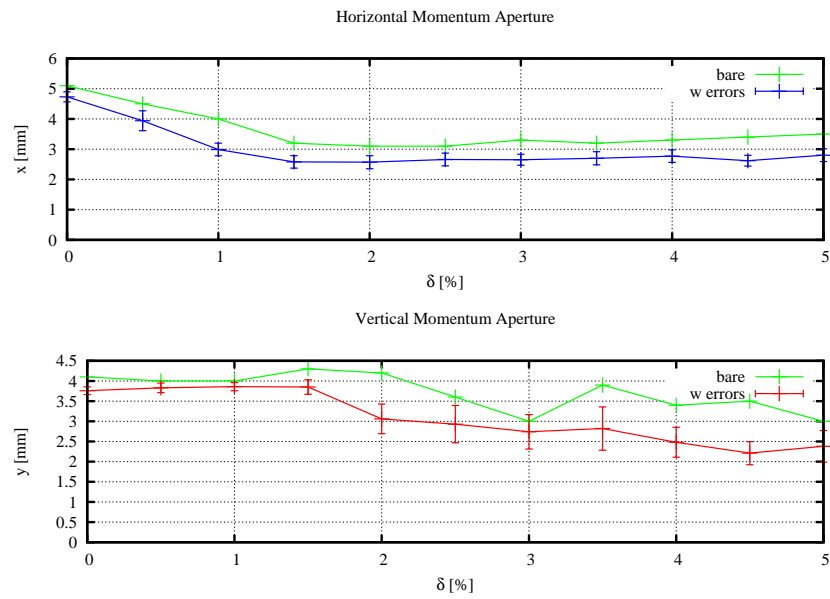


Figure 20: Off-Momentum Dynamic Aperture for Bare and Real Lattice (4096 turns).

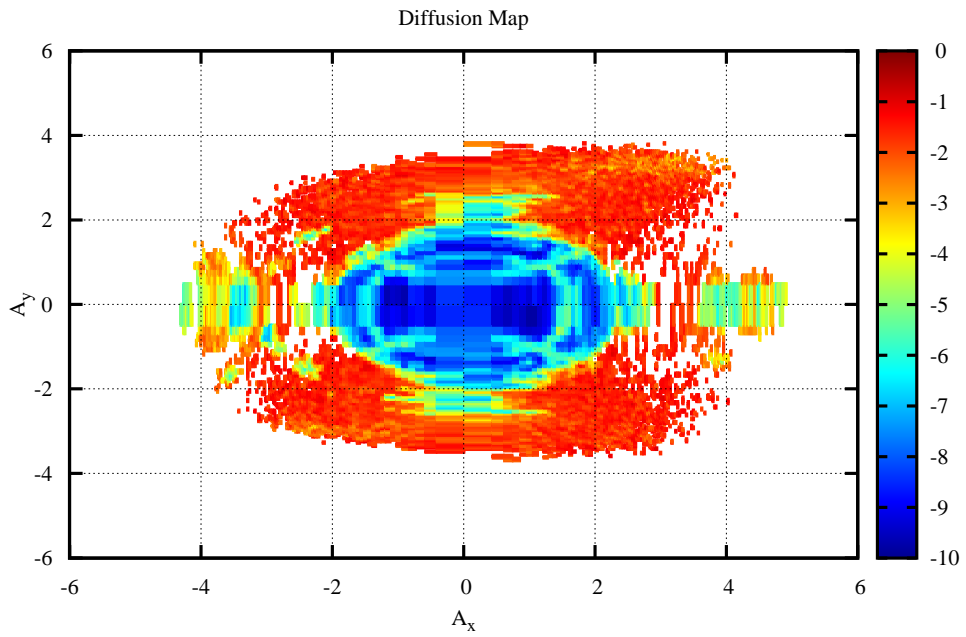
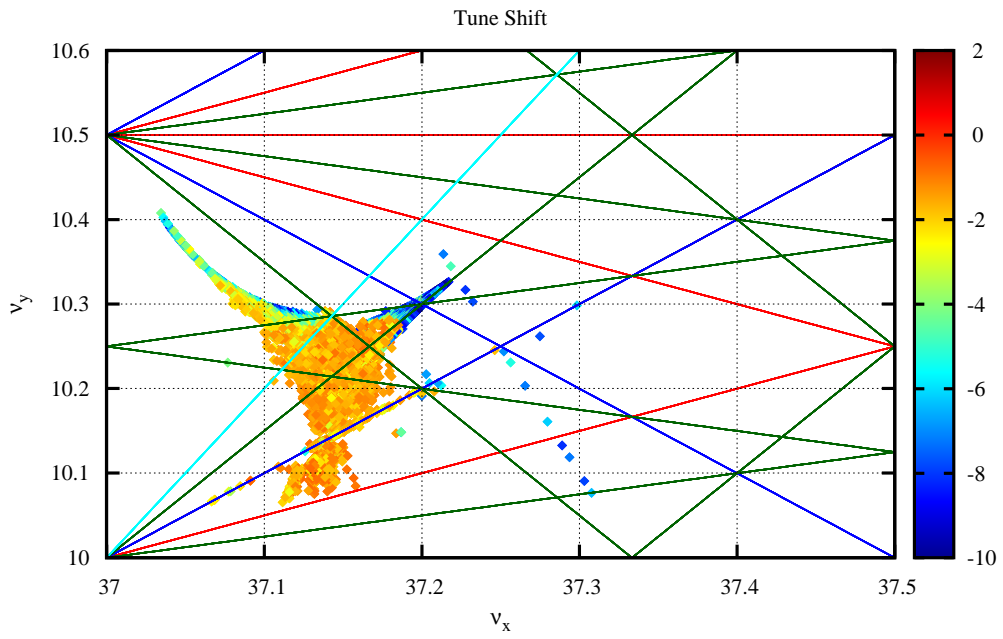


Figure 21: On-Momentum Frequency Map for Real Lattice (4,128 turns).

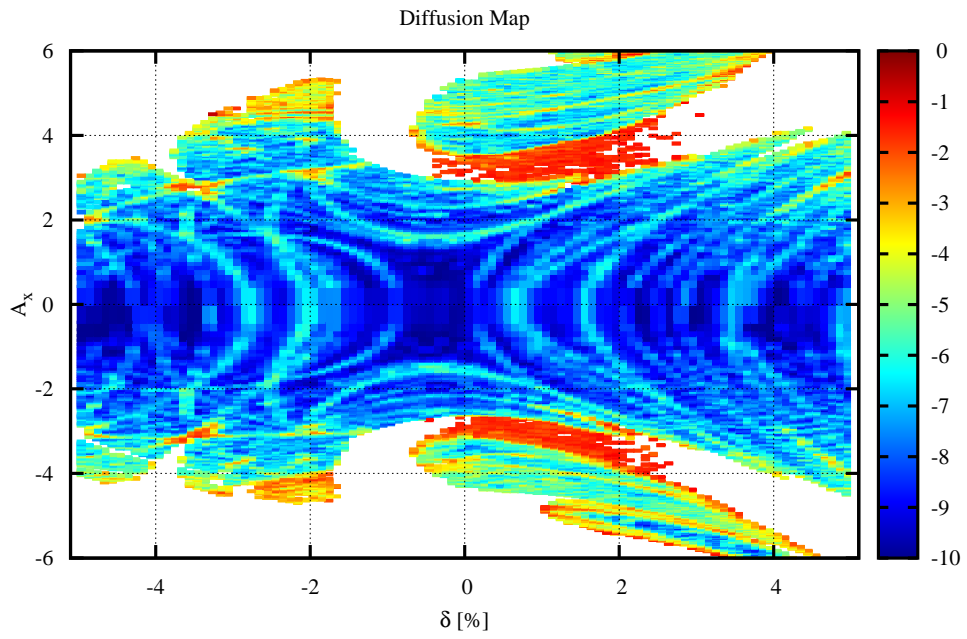
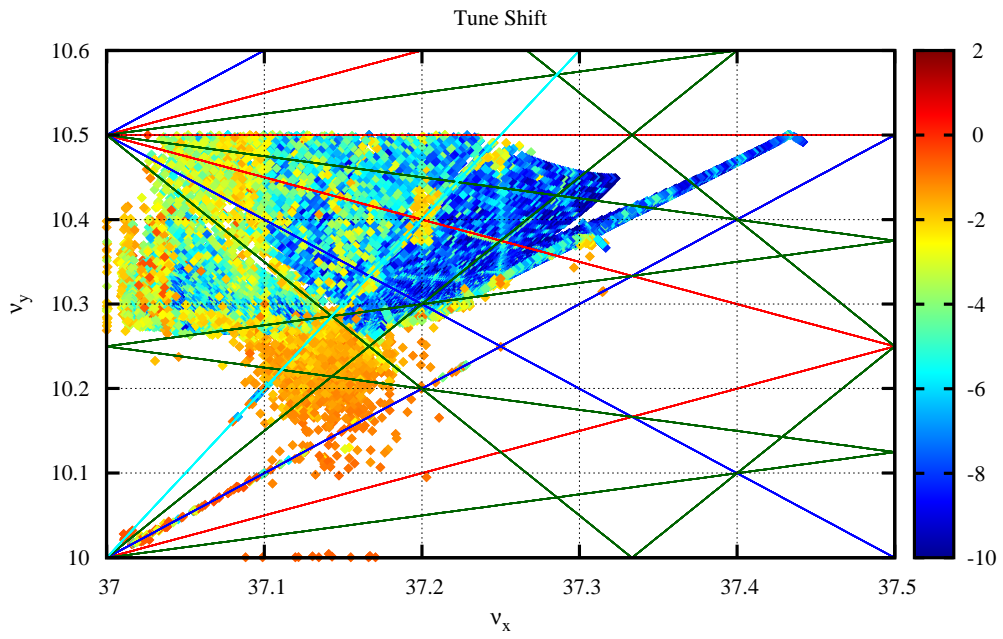


Figure 22: Off-Momentum Frequency Map for Real Lattice (4,128 turns).

B Engineering Tolerances

The mechanical mis-alignment and magnetic multipole tolerances are summarized in in Tabs. 5-6. For the guidelines and what was achieved for SLS see ref. [42–45].

Type	$[\Delta x, \Delta y]$ rms (μm)	Roll rms (mrad)
(Girder)	(25)	(0.2)
Dipole	20	0.2
Quadrupole	20	0.2
Sextupole	20	0.2
Octupole	25	0.2
BPM	5	0.01

Table 5: Mechanical Alignment Tolerances.

Quadrupoles ($R_{\text{ref}} = 10 \text{ mm}$)	Random (10^{-4})	Quadrupoles ($R_{\text{ref}} = 10 \text{ mm}$)	Systematic (10^{-4})
n	$[\Delta B_n, \Delta A_n]$	n	$[\Delta B_n, \Delta A_n]$
2	5.0, 0.0	6	2.0, 0.0
3	1.1, 1.1	10	2.0, 0.0
4	0.3, 0.2	14	2.0, 0.0
6	0.03, 0.0		

Table 6: Tolerances for Random and Systematic Multipoles in the Quadrupoles.

Sextupoles ($R_{\text{ref}} = 10 \text{ mm}$)	Random (10^{-4})	Sextupoles ($R_{\text{ref}} = 10 \text{ mm}$)	Systematic (10^{-4})
n	$[\Delta B_n, \Delta A_n]$	n	$[\Delta B_n, \Delta A_n]$
3	5.0, 0.0	9	3.0, 0.0
4	2.0, 2.0	15	3.0, 0.0
5	0.6, 0.0	21	3.0, 0.0

Table 7: Tolerances for Random and Systematic Multipoles in the Sextupoles.

Octupoles ($R_{\text{ref}} = 10 \text{ mm}$)	Random (10^{-4})
n	$[\Delta B_n, \Delta A_n]$
4	5.0, 0.0

Table 8: Tolerances for Random Multipoles in the Octupoles.

C Round Beam: The Möbius Ring

One way to implement a round beam is by implementing a Möbius ring [46, 47]. However, since this implies introducing a strong linear coupling between the horizontal and vertical planes, the related linear coupling resonances $\nu_x \pm \nu_y$ are likely to degrade the performance of a state-of-the-arts synchrotron light source lattice. So, for a robust approach, to e.g. mitigate the effect of Intrabeam scattering (IBS), one may instead generate a dispersion wave [48, 49].

For the former approach, a Möbius ring is obtained by inserting a twist section

$$M_{\text{Twist}} = \begin{bmatrix} 0 & \pm I \\ I & 0 \end{bmatrix} \quad (63)$$

to a lattice with mid-plane symmetry and the linear map

$$M_{x,y} = \begin{bmatrix} \cos(\mu_{x,y}) + \alpha_{x,y} \sin(\mu_{x,y}) & \beta_{x,y} \sin(\mu_{x,y}) \\ -\gamma_{x,y} \sin(\mu_{x,y}) & \cos(\mu_{x,y}) - \alpha_{x,y} \sin(\mu_{x,y}) \end{bmatrix}, \quad (64)$$

one obtains

$$M = \begin{bmatrix} 0 & \pm M_y \\ M_x & 0 \end{bmatrix}. \quad (65)$$

Averaging over two turns around the lattice with the twist section one obtains

$$\tilde{\varepsilon}_x = \tilde{\varepsilon}_y = \tau (\langle \mathcal{H}_x D_\delta \rangle + \langle \mathcal{H}_y D_\delta \rangle) = \frac{J_\delta \tau \delta}{J_x + J_y} (\langle \mathcal{H}_x D_\delta \rangle + \langle \mathcal{H}_y D_\delta \rangle) = \frac{J_x \varepsilon_x + J_y \varepsilon_y}{J_x + J_y} \quad (66)$$

since

$$\frac{1}{\tau} = \frac{1}{\tau_x} + \frac{1}{\tau_y} = \frac{J_x + J_y}{J_\delta \tau \delta}. \quad (67)$$

Hence, for an initial lattice with mid-plane symmetry

$$\tilde{\varepsilon}_x = \tilde{\varepsilon}_y = \frac{\varepsilon_x}{1 + \frac{J_y}{J_x}}. \quad (68)$$